The Astrophysical Journal, 849:91 (26pp), 2017 November 10 https://doi.org/10.3847/1538-4357/aa9185

Physical Properties of 15 Quasars at $z \gtrsim 6.5$

C. Mazzucchelli[1], E. Bañados[1,2,12], B. P. Venemans[1], R. Decarli[1], E. P. Farina[1], F. Walter[1], A.-C. Eilers[1], H.-W. Rix[1], R. Simcoe[3], D. Stern[4], X. Fan[5], E. Schlafly[6,13], G. De Rosa[7], J. Hennawi[1,8], K. C. Chambers[9], J. Greiner[10], W. Burgett[9], P. W. Draper[11], N. Kaiser[9], R.-P. Kudritzki[9], E. Magnier[9], N. Metcalfe[11], C. Waters[9], and R. J. Wainscoat[9]

[1] Max-Planck-Institut für Astronomie, Königstuhl 17, D-69117 Heidelberg, Germany
[2] The Observatories of the Carnegie Institute of Washington, 813 Santa Barbara Street, Pasadena, CA 91101, USA
[3] MIT-Kavli Center for Astrophysics and Space Research, 77 Massachusetts Avenue, Cambridge, MA 02139, USA
[4] Jet Propulsion Laboratory, California Institute of Technology, 4800 Oak Grove Drive, Pasadena, CA 91109, USA
[5] Steward Observatory, The University of Arizona, 933 North Cherry Avenue, Tucson, AZ 857210065, USA
[6] Lawrence Berkeley National Laboratory, Berkeley, CA 94720, USA
[7] Space Telescope Science Institute, 3700 San Martin Drive, Baltimore, MD 21218, USA
[8] Physics Department, University of California, Santa Barbara, CA 93106-9530, USA
[9] Institute for Astronomy, University of Hawaii, 2680 Woodlawn Drive, Honolulu, HI 96822, USA
[10] Max-Planck-Institut für extraterrestrische Physik, Giessenbachstrasse 1, D-85748 Garching, Germany
[11] Department of Physics, Durham University, South Road, Durham DH1 3LE, UK
Received 2017 June 9; revised 2017 September 22; accepted 2017 October 2; published 2017 November 6

Abstract

Quasars are galaxies hosting accreting supermassive black holes; due to their brightness, they are unique probes of the early universe. To date, only a few quasars have been reported at $z > 6.5$ (<800 Myr after the big bang). In this work, we present six additional $z \gtrsim 6.5$ quasars discovered using the Pan-STARRS1 survey. We use a sample of 15 $z \gtrsim 6.5$ quasars to perform a homogeneous and comprehensive analysis of this highest-redshift quasar population. We report four main results: (1) the majority of $z \gtrsim 6.5$ quasars show large blueshifts of the broad C IV λ1549 emission line compared to the systemic redshift of the quasars, with a median value $\sim$3$\times$ higher than a quasar sample at $z \sim 1$; (2) we estimate the quasars' black hole masses ($M_{\rm BH} \sim (0.3\text{–}5) \times 10^9\ M_\odot$) via modeling of the Mg II λ2798 emission line and rest-frame UV continuum and find that quasars at high redshift accrete their material (with $\langle (L_{\rm bol}/L_{\rm Edd}) \rangle = 0.39$) at a rate comparable to a luminosity-matched sample at lower redshift, albeit with significant scatter (0.4 dex); (3) we recover no evolution of the Fe II/Mg II abundance ratio with cosmic time; and (4) we derive near-zone sizes and, together with measurements for $z \sim 6$ quasars from recent work, confirm a shallow evolution of the decreasing quasar near-zone sizes with redshift. Finally, we present new millimeter observations of the [C II] 158 μm emission line and underlying dust continuum from NOEMA for four quasars and provide new accurate redshifts and [C II]/infrared luminosity estimates. The analysis presented here shows the large range of properties of the most distant quasars.

Key words: galaxies: high-redshift – quasars: general

1. Introduction

Quasars are massive galaxies hosting fast accreting supermassive black holes ($\gtrsim 10^8\ M_\odot$) in their centers. They are the most luminous, nontransient sources in the sky, and hence they can be observed at extremely large cosmological look-back times ($z > 6$, <1 Gyr after the big bang), where normal star-forming galaxies are often too faint to be comprehensively studied. Quasars are therefore unique lighthouses, illuminating a number of open issues regarding the very early stages of the universe.

First, their very presence at such primeval cosmic times challenges models of the formation and growth of supermassive black holes (e.g., Volonteri 2010; Latif & Ferrara 2016). The current preferred models include the formation of black hole seeds from the direct collapse of massive gaseous reservoirs (e.g., Haehnelt & Rees 1993; Latif & Schleicher 2015), the collapse of Population III stars (e.g., Bond et al. 1984; Alvarez et al. 2009; Valiante et al. 2016), the co-action of dynamical processes, gas collapse and star formation (e.g., Devecchi & Volonteri 2009), or the rapid growth of stellar-mass seeds via episodes of super-Eddington, radiatively inefficient accretion (e.g., Alexander & Natarajan 2014; Madau et al. 2014; Pacucci et al. 2015; Lupi et al. 2016; Pezzulli et al. 2016; Volonteri et al. 2016; Begelman & Volonteri 2017). From black hole growth theory, we know that black holes can evolve very rapidly from their initial seed masses $M_{\rm BH,seed}$ to the final mass $M_{\rm BH,f}$ ($M_{\rm BH,f} \sim M_{\rm BH,seed}\ e^{9\times t\ [\rm Gyr]/0.45}$, assuming accretion at the Eddington limit and an efficiency of 10%; Volonteri & Rees 2005). For instance, in the seemingly short redshift range $z \sim 6.0$–6.5, corresponding to ~90 Myr, a black hole can grow by a factor of 6. From the observational perspective, the discovery of quasars at $z \gtrsim 6.5$ can give stronger constraints on the nature of black hole seeds than the quasar population at $z \sim 6$.

Moreover, several studies show that quasars at $z \sim 6$ are hosted in massive, already chemically evolved galaxies (e.g., Barth et al. 2003; Stern et al. 2003; Walter et al. 2003; De Rosa et al. 2011). These galaxies contain a conspicuous amount of cool gas and dust, as observed through the detection of the bright [C II] 158 μm emission line and its underlying continuum, falling in the millimeter regime at $z \gtrsim 5.5$ (e.g., Maiolino et al. 2009; Walter et al. 2009; Wang et al. 2013; Willott et al. 2015; Venemans et al. 2016, R. Decarli et al., in

[12] Carnegie-Princeton Fellow.
[13] Hubble Fellow.

preparation; for a review see Carilli & Walter 2013). Sampling the cool gas content of high-redshift quasar host galaxies with millimeter observations is therefore of great importance in pinpointing the gas content of massive galaxies in the universe at early ages.

Finally, the bright quasar emission has been used as background light to study the conditions of the intergalactic medium (IGM) at the epoch of reionization (EoR), when the universe transitioned from being neutral to the current, mostly ionized state. The current best constraints on the EoR are derived from the cosmic microwave background (CMB) and quasar spectra. In the former case, recent CMB measurements by the Planck Collaboration et al. (2016) set a redshift of $z \sim 8.8$ for the EoR (under the hypothesis that the reionization is instantaneous). In the latter case, several studies investigate the evolution of the IGM ionized fraction during the EoR through high-z quasar emission, e.g., by measuring transmission spikes in the Lyα forest (e.g., Fan et al. 2006; Becker et al. 2015; Barnett et al. 2017), and by computing the Lyα power spectrum (e.g., Palanque-Delabrouille et al. 2013). Another method is based on measurements of near-zone sizes, e.g., regions around quasars that are ionized by emission from the central objects. Their evolution with redshift has been studied to investigate the evolution of the IGM neutral fraction with cosmic time (e.g., Fan et al. 2006; Carilli et al. 2010; Venemans et al. 2015a). However, the modest-sized and nonhomogeneous quasar samples at hand, large errors due to uncertain redshifts, and the limited theoretical models available have inhibited our understanding of these measurements to date, i.e., do they trace the evolution of the ionized gas fraction, or are they dominated by degeneracies (e.g., quasar lifetimes)? Recently, Eilers et al. (2017) addressed some of these caveats, deriving near-zone sizes of 34 quasars at $5.77 \lesssim z \lesssim 6.54$. They find a less pronounced evolution of near-zone radii with redshift than what has been reported by previous studies (e.g., Carilli et al. 2010; Venemans et al. 2015a). Measurements from quasars at higher redshift are required to test whether this trend holds far deeper into the EoR. To further progress in all the issues reported above, it is of paramount importance to identify new quasars, especially at the highest redshifts, and study their properties comprehensively.

Color selection techniques, which rely on multiwavelength broadband observations, are among the most commonly used methods to find high-redshift quasars. The quasar flux at wavelengths shorter than the Lyα emission line (at rest-frame $\lambda_{\rm rf} = 1215.67$ Å) is absorbed by the intervening neutral medium, causing an extremely red $(i-z)$ or $(z-y)$ color if the source is at $z \gtrsim 6$ (i-dropouts) or $z \gtrsim 6.4$ (z-dropouts), respectively. In the past two decades ~200 quasars have been discovered at $5.4 < z < 6.4$, mainly thanks to the advent of large-area surveys, e.g., the Sloan Digital Sky Survey (SDSS; Fan et al. 2000, Fan et al. 2003, 2006, Jiang et al. 2016; Wang et al. 2016, Wang et al. 2017), the Canada–France High-redshift Quasar Survey (CFHQS; Willott et al. 2007, 2009, 2010b, 2013), the UK Infrared Deep Sky Server (UKIDSS; Venemans et al. 2007; Mortlock et al. 2009), the Dark Energy Survey (DES; Reed et al. 2015, Reed et al. 2017), the Very Large Telescope Survey Telescope (VST) ATLAS Survey (Carnall et al. 2015), the ESO public Kilo-Degree Survey (KiDS; Venemans et al. 2015b), and the Panoramic Survey Telescope and Rapid Response System (Pan-STARRS1 or PS1; Morganson et al. 2012; Bañados et al. 2014, 2015b, 2016). However, the search for sources at even higher redshift ($z \gtrsim 6.4$; age of the universe <0.80 Gyr) has been extremely challenging, and only a few quasars have been discovered at such a distance prior to the results presented here: three from the VISTA Kilo-Degree Infrared Galaxy Survey (VIKING; Venemans et al. 2013), four from PS1 (Venemans et al. 2015a; Tang et al. 2017), and one from the Subaru Hyper Suprime-Cam-SPP Survey (HSC-SPP; Matsuoka et al. 2016, Matsuoka et al. 2017); so far, only one quasar has been found at $z > 7$ in the UKIDSS (Mortlock et al. 2011).

In this work, we describe our search for $z \gtrsim 6.5$ quasars in the Pan-STARRS1 survey (Kaiser et al. 2002, 2010; Chambers et al. 2016; Flewelling et al. 2016; Magnier et al. 2016a, 2016b, 2016c; Waters et al. 2016), which imaged the entire sky at decl. $> -30°$ in five filters ($g_{\rm P1}$, $r_{\rm P1}$, $i_{\rm P1}$, $z_{\rm P1}$, $y_{\rm P1}$). We use here the third internal release of the 3π stacked catalog (PS1 PV3, in the internal naming convention). The 5σ AB magnitude limits are $(g_{\rm P1}, r_{\rm P1}, i_{\rm P1}, z_{\rm P1}, y_{\rm P1}) = (23.3, 23.2, 23.1, 22.4, 21.4)$.[14] We present six newly discovered z-dropouts from this search, at $z \sim 6.5$ ($6.42 < z < 6.59$). We then provide a comprehensive analysis of the sample of the known $z \gtrsim 6.5$ quasars (15 objects).[15] Our goal is to implement a coherent investigation of several key quasar properties (i.e., black hole mass, accretion rate, near-zone size, and infrared luminosity) and compare them to lower-redshift samples. The paper is organized as follows: in Section 2 we present our method for selecting quasar candidates from the PS1 PV3 database together with other publicly available surveys; in Section 3 we report the imaging and spectroscopic follow-up observations obtained to confirm the quasar nature of our candidates; we also present new near-IR (NIR)/optical spectroscopy of quasars from the literature and new observations of the [C II] 158 μm emission line and underlying continuum for four quasars. In Section 4 we discuss the properties of each of the new PS1 quasars presented here. In Section 5 we present our quasar sample at $z \gtrsim 6.5$: redshifts (Section 5.1), absolute magnitudes at rest-frame wavelength 1450 Å (Section 5.2), C IV λ1549.06 broad emission line characteristics (Section 5.4), black hole masses, bolometric luminosities and accretion rates (Sections 5.3–5.6), iron-to-magnesium flux ratios (Section 5.8), infrared and [C II] luminosities (Section 5.9), and near-zone sizes (Section 5.10). Finally, in Section 6 we discuss and summarize our findings. The International Astronomical Union imposes in its naming convention that all nontransient sources discovered in the PS1 survey are named "PSO JRRR.rrrr ± DD.dddd," with RRR.rrrr and DD.dddd right ascension and declination in decimal degrees (J2000), respectively. For simplicity, in this paper we will refer to the PS1 quasars as "PSO RRR+DD" and to sources from other surveys, e.g., VIKING, UKIDSS, and HSC, as "VIK hhmm," "ULAS hhmm," and "HSC hhmm."

We consider throughout the paper the PS1 point-spread function (PSF) magnitudes ($g_{\rm P1}$, $r_{\rm P1}$, $i_{\rm P1}$, $z_{\rm P1}$, $y_{\rm P1}$). The magnitudes reported in this work are all in the AB system. We use a ΛCDM cosmology with $H_0 = 70$ km s^{-1} Mpc^{-1}, $\Omega_{\rm m} = 0.3$, and $\Omega_\Lambda = 0.7$.

[14] See also Chambers et al. (2016), Table 11.

[15] We do not consider the quasars VDES J0224–4711 ($z = 6.50$; Reed et al. 2017), DELS J104819.09–010940.2 ($z = 6.63$; Wang et al. 2017), and J1429–0104 ($z = 6.80$; Matsuoka et al. 2017), which were reported during the final stages of the preparation of this manuscript.

2. Candidate Selection

We perform a search for z-dropouts in the Pan-STARRS1 survey using the PS1 PV3 catalog (see Section 1). We follow and expand the selection illustrated both in Bañados et al. (2016), which was focused on lower-redshift objects ($z \sim 6$), and in Venemans et al. (2015a).

Samples of high-redshift quasar candidates selected through broadband imaging and optical color criteria are highly contaminated by the numerous cool dwarf stars in our Galaxy (mainly M/L/T dwarfs), which present similar colors and morphology. We therefore compile our sample and clean it from contaminants through the following steps:

1. initial search based on the PS1 PV3 catalog and cross-match with known cool dwarf and quasar lists;
2. cross-match with other infrared public surveys;
3. forced photometry on the stacked and single-epoch PS1 images;
4. fit of the spectral energy distribution (SED); and
5. visual inspection.

Afterward, we follow up the selected candidates with dedicated photometric campaigns, followed by spectroscopy of the remaining targets to confirm (or discard) their quasar nature (see Section 3).

2.1. PS1 Catalog

The flux of high-redshift quasars at wavelengths shorter than the Lyα emission line is strongly absorbed by the intervening IGM. Therefore, we expect to recover little or no flux in the bluer bands and to observe a strong break of the continuum emission. We base our selection of z-dropouts on the $y_{\rm P1}$ magnitude and require the objects to have $\rm S/N(y_{P1}) > 7$, where S/N is the signal-to-noise ratio. Then, we require $\rm S/N(g_{P1}, r_{P1}) < 3$ and $\rm S/N(i_{P1}) < 5$, or, in case the latter criterion is not satisfied, a color $(i_{\rm P1} - y_{\rm P1}) > 2.2$. Furthermore, we require a $(z_{\rm P1} - y_{\rm P1})$ color criterion as

$$\rm S/N(z_{P1}) > 3 \quad and \quad z_{P1} - y_{P1} > 1.4 \quad or \tag{1}$$

$$\rm S/N(z_{P1}) < 3 \quad and \quad z_{P1,lim} - y_{P1} > 1.4. \tag{2}$$

In order to reject objects with an extended morphology, we require

$$|y_{\rm P1} - y_{\rm P1,aper}| < 0.3, \tag{3}$$

where $y_{\rm P1,aper}$ is the aperture magnitude in the PS1 catalog. This cut was implemented based on a test performed on a sample of spectroscopically confirmed stars and galaxies (from SDSS-DR12; Alam et al. 2015) and quasars at $z > 2$ (from SDSS-DR10; Pâris et al. 2014). Using this criterion, we are able to select a large fraction of point-like sources (83% of quasars and 78% of stars) and reject the majority of galaxies (94%; see Bañados et al. 2016, for more details on this approach). Additionally, we discard objects based on the quality of the $y_{\rm P1}$-band image using the flags reported in the PS1 catalog (e.g., we require that the peak of the object is not saturated, and that it not land off the edge of the chip or on a diffraction spike; for a full summary, see Bañados et al. 2014, Appendix A). We require also that 85% of the expected PSF-weighted flux in the $z_{\rm P1}$ and $y_{\rm P1}$ bands falls in a region of valid pixels (the catalog entry `PSF_QF` >0.85). We exclude objects in regions of high Galactic extinction ($E(B - V) > 0.3$), following the extinction map of Schlegel et al. (1998); we also exclude the area close to M31 (00:28:04 < R.A. < 00:56:08 and 37° < decl. < 43°). We clean the resulting sample by removing known quasars at $z \geqslant 5.5$ (see references in Bañados et al. 2016, Table 7). The total number of candidates at this stage is ~781,000.

2.2. Cross-match with Public Surveys

We take advantage of the information provided by other public surveys, when their sky coverage overlaps with Pan-STARRS1. We here consider solely the sources with a detection in the *WISE* catalog.

2.2.1. ALLWISE Survey

We consider the ALLWISE catalog,[16] resulting from the combination of the all-sky *Wide-field Infrared Survey Explorer* mission (*WISE* mission; Wright et al. 2010) and the NEOWISE survey (Mainzer et al. 2011). The 5σ limiting magnitudes are $W1 = 19.3$, $W2 = 18.9$, and $W3 = 16.5$. We use a match radius of 3″, requiring S/N > 3 in $W1$ and $W2$. We further impose

$$-0.2 < W1 - W2 < 0.86, \tag{4}$$

$$W1 - W2 > (-1.45 \times ((y_{\rm P1} - W1) - 0.1) - 0.6). \tag{5}$$

For candidates with S/N($W3$) >3 we prioritize sources with $W2 - W3 > 0$. These selection criteria help exclude the bulk of the L-dwarf population (Bañados et al. 2016). The aforementioned color criteria were solely used to prioritize sources for follow-up observations, but not to reject them.

2.2.2. UKIDSS and VHS

We cross-match our sample using a 2″ matching radius with the UKIDSS Large Area Survey (UKIDSS LAS; Lawrence et al. 2007) data release 10 (http://surveys.roe.ac.uk/wsa/dr10plus_release.html) and the VISTA Hemisphere Survey (VHS; McMahon et al. 2013). UKIDSS and VHS provide Y, J, H, and K images over areas of ~4000 and ~8000 deg^2, respectively. The UKIDSS mapped regions of the sky within coordinates 00:32:04 < R.A. < 01:04:07, −1°.0 < decl. < 16° and 00:32:04 < R.A. < 01:04:07, 20° < decl. < 40°, to 5σ limiting magnitudes of $Y = 20.8$, $J = 20.5$, $H = 20.2$, and $K = 20.1$. The VHS aims to cover the southern hemisphere, avoiding the Milky Way footprint, and to reach a depth ~30 times fainter than the Two Micron All Sky Survey. In this work, we reject objects from our initial selection in case they were detected in these catalogs and had $Y - J > 0.6$ and/or $y_{\rm P1} - J > 1$ (e.g., typical colors of brown dwarfs; see Best et al. 2013).

2.2.3. DECaLS

The Dark Energy Camera Legacy Survey (DECaLS[17]) is an ongoing survey that will image ~6700 deg^2 of the sky in the northern hemisphere, up to decl. < 30°, in $g_{\rm decam}$, $r_{\rm decam}$, and $z_{\rm decam}$, using the Dark Energy Camera on the Blanco Telescope. We consider the Data Release 2 (DR2[18]), which covers only a

[16] http://wise2.ipac.caltech.edu/docs/release/allwise/
[17] http://legacysurvey.org/decamls/
[18] http://legacysurvey.org/dr2/description/

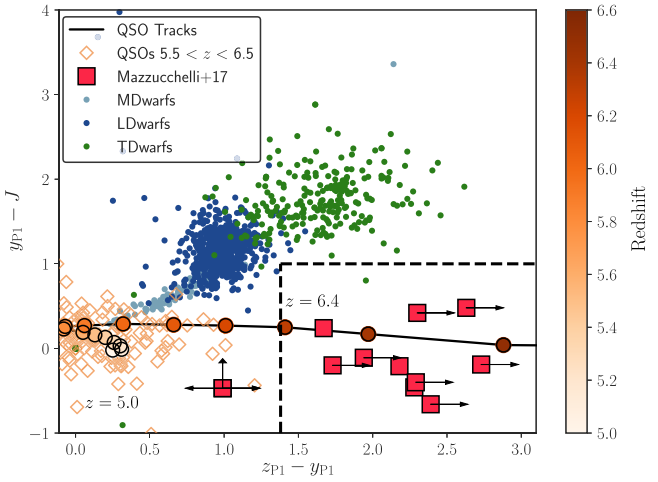

Figure 1. Color–color diagram ($y_{P1} - J$ vs. $z_{P1} - y_{P1}$) used in our search for high-redshift quasars. We show the predicted quasar track (black solid line and circles color-coded with respect to redshift, in steps of $\Delta z = 0.1$), obtained by convolving the high-redshift quasar composite template reported by Bañados et al. (2016; see also Section 2.4) with the filters considered here. Observed colors of L/T dwarfs, taken from the literature (see text for references), are reported with blue and green filled circles, while we consider for M dwarfs the colors calculated convolving a collection of spectra with the filters used here (see Section 2.4). We show also the location of known quasars at $5.5 < z < 6.5$ (orange open diamonds; see Section 5.2 for references) and the objects studied in this work (red squares, with black right-pointing arrows in case they only have lower limits in the z_{P1} band from the PS1 PV3 catalog; see Table 3). We do not show quasars from the VIKING survey, which are not present in the PS1 catalog, and PSO 006+39, for which we do not possess J-band photometry. For HSC 1205 we use the 3σ limits in z_{P1} and y_{P1} obtained from the forced photometry on the PS1 PV3 stacked images. Our selection box is highlighted with dashed black lines.

fraction of the proposed final area (2078 deg^2 in g_{decam}, 2141 deg^2 in r_{decam} and 5322 deg^2 in z_{decam}) but is deeper than PS1 ($g_{decam,5\sigma} = 24.7$, $r_{decam,5\sigma} = 23.6$, $z_{decam,5\sigma} = 22.8$). We use a match radius of 2″. We reject all objects detected in g_{decam} and/or r_{decam}, or that present an extended morphology (e.g., with catalog entry `type` different than "PSF").

In Figure 1 we show one of the color–color plots ($y_{P1} - J$ versus $z_{P1} - y_{P1}$) used at this stage of the candidate selection.

2.3. Forced Photometry on PS1 Images

Next, we perform forced photometry on both the stacked and single-epoch images from PS1 of our remaining candidates. This is to confirm the photometry from the PS1 PV3 stacked catalog and to reject objects showing a large variation in the flux of the single-epoch images that would most probably indicate spurious detections (for further details on the cuts used at this stage, see Bañados et al. 2014).

2.4. SED Fit

We implement an SED fitting routine to fully exploit all the multiwavelength information provided by the surveys described in Sections 2.1 and 2.2. We compare the observations of our candidates with synthetic fluxes, obtained by interpolating quasar and brown dwarf spectral templates through different filter curves, in the 0.7–4.6 μm observed wavelength range.

We consider 25 observed brown dwarf spectra taken from the SpeX Prism Library[19] (Burgasser 2014), and representative of typical M4–M9, L0–L9, and T0–T8 stellar types. These spectra cover the wavelength interval 0.65–2.55 μm (up to K band). The corresponding $W1$ (3.4 μm) and $W2$ (4.6 μm) magnitudes are obtained following Skrzypek et al. (2015), who exploit a reference sample of brown dwarfs with known spectral and photometric information to derive various color relations. For each brown dwarf template, we derive the *WISE* magnitudes using the synthetic K magnitude and scaling factors (K_W1 and $W1\_W2$), which depend on the stellar spectral type.[20] We apply the following relations:

$$W1 = K - K\_W1 - 0.783, \quad (6)$$

$$W2 = W1 - W1\_W2 - 0.636. \quad (7)$$

For the quasar models, we use four different observed composite spectra: the SDSS template, obtained from a sample of $1 \lesssim z \lesssim 2$ quasars (Selsing et al. 2016), and three composites of $z \gtrsim 5.6$ quasars by Bañados et al. (2016), the first one based on 117 sources (from PS1 and other surveys), the second obtained considering only the 10% of objects with the largest rest-frame Lyα+N V equivalent width (EW), and the last using the 10% of sources with the smallest EW (Lyα +N V). These different templates allow us to take into account color changes due to the Lyα emission line strength. However, the three models from Bañados et al. (2016) cover only to rest-frame wavelength $\lambda_{rf} \sim 1500$ Å, so we use the template from Selsing et al. (2016) to extend coverage into the NIR region. We shift all the quasar templates over the redshift interval $5.5 \leqslant z \leqslant 9.0$, with $\Delta z = 0.1$. We consider the effect of the IGM absorption on the SDSS composite spectrum using the redshift-dependent recipe provided by Meiksin (2006). For the quasar templates from Bañados et al. (2016), we implement the following steps: we correct each model for the IGM absorption as calculated at redshift $z = z_{median}$ of the quasars used to create the composite, obtaining the reconstructed emitted quasar spectra. Then, we re-apply the IGM absorption to the corrected models at each redshift step, again using the method by Meiksin (2006). The total number of quasar models is 140.

For each quasar candidate from our selection, after having normalized the brown dwarf and quasar templates to the candidate observed flux at y_{P1}, we find the best models that provide the minimum reduced χ^2, $\chi^2_{b,\min,r}$ and $\chi^2_{q,\min,r}$, for brown dwarf and quasar templates, respectively. We assume that the candidate is best fitted by a quasar template if $R = \chi^2_{q,\min,r} / \chi^2_{b,\min,r} < 1$. In our search, we prioritize for further follow-up observation sources with the lowest R values. Though we do not reject any object based on this method, candidates with $R > 1$ were given the lowest priority. An example of the best quasar and brown dwarf models for one of our newly discovered quasars is shown in Figure 2.

Finally, we visually inspect all the stacked and single-epoch PS1 frames, together with the images from the other public surveys, when available (~4000 objects). This is to reject nonastronomical or spurious sources (e.g., CCD defects, hot pixels, moving objects). We then proceed with follow-up of the remaining targets (~1000).

3. Observations

We first obtain imaging follow-up observations of our quasar candidates, and then we take spectra of the most promising objects.

[19] http://pono.ucsd.edu/~adam/browndwarfs/spexprism/

[20] The scaling factors K_W1 and $W1\_W2$ for the different M/T/L stellar types can be found in Table 1 of Skrzypek et al. (2015).

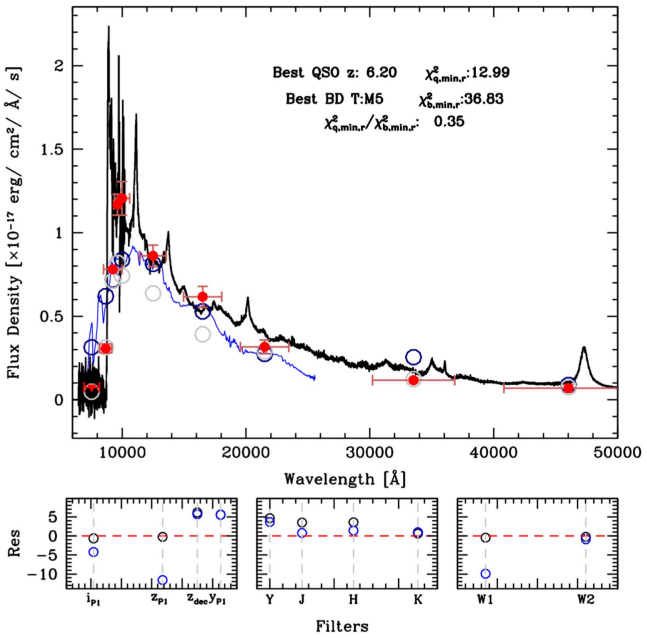

Figure 2. Example of SED fit for one of our candidates, confirmed to be a quasar at $z \sim 6.4377$ (PSO 183+05; see Table 5). In the top panel, we show the photometric information taken from public surveys (red circles and downward-pointing arrows in case of nondetections at 3σ significance; see Section 2), the best quasar template (the weak-lined PS1 quasar template at $z = 6.2$; black solid line), and the best brown dwarf template (M5; blue solid line). The synthetic fluxes of the best quasar and brown dwarf templates, obtained by convolving the models to the filters considered here, are shown with light-gray and blue open circles, respectively. In the bottom panels, the residuals, e.g., $(\mathrm{flux}_{\mathrm{data},f} - \mathrm{flux}_{\mathrm{best\ model},f,q/b})/\sigma_f$, are displayed, for each f band used here. Blue and black open circles indicate the best brown dwarf and quasar template, respectively.

3.1. Imaging and Spectroscopic Confirmation

We perform follow-up imaging observations in order both to confirm the catalog magnitudes and to obtain missing NIR and deep optical photometry, crucial in identifying contaminant foreground objects.

We take advantage of different telescopes and instruments: MPG 2.2 m/GROND (Greiner et al. 2008), NTT/EFOSC2 (Buzzoni et al. 1984), NTT/SofI (Moorwood et al. 1998), du Pont/Retrocam,[21] Calar Alto 3.5 m/Omega2000 (Bailer-Jones et al. 2000), Calar Alto 2.2 m/CAFOS.[22] In Table 1 we report the details of our campaigns, together with the filters used.

The data were reduced using standard data reduction procedures (Bañados et al. 2014). We refer to Bañados et al. (2016) for the color conversions used to obtain the flux calibration. In case we collect new J-band photometry for objects undetected or with low S/N in NIR public surveys, we consider as good quasar candidates the ones with $-1 < y_{P1} - J < 1$, while the sources with very red or very blue colors were considered to be stellar contaminants or spurious/moving objects, respectively. For sources with good NIR colors (from either public surveys or our own follow-up photometry), we collected deep optical imaging.

We then took spectra of all the remaining promising candidates using VLT/FORS2 (Appenzeller et al. 1998), P200/DBSP (Oke & Gunn 1982), MMT/Red Channel (Schmidt et al. 1989), Magellan/FIRE (Simcoe et al. 2008), and LBT/MODS (Pogge et al. 2010) spectrographs. Standard techniques were used to reduce the data (see Venemans et al. 2013; Bañados et al. 2014, 2016; Chen et al. 2016). Six objects out of nine observed candidates were confirmed as high-redshift quasars: we present them and provide further details in Section 4. We list the spectroscopically rejected objects (Galactic sources) in Appendix B. Further information on these observations, together with the additional spectroscopic observations for other objects in our quasar sample (see Section 3.2), are reported in Table 2. In Table 3, we provide photometric data from catalogs for all the objects in our high-redshift quasar sample. Also, photometry from our own follow-up campaigns for the new six quasars is listed in Table 4. Table 11 in Appendix A lists the information (central wavelength and width, λ_c and $\Delta\lambda$) of the various filters used in this work, from both public surveys and follow-up photometry.

3.2. Spectroscopic Follow-up of $z \gtrsim 6.44$ Quasars

Once the high-redshift quasar nature of candidates is confirmed, we include them in our extensive campaign of follow-up observations aimed at characterizing quasars at the highest redshifts.

Here we present new optical/NIR spectroscopic data for nine quasars, the six objects newly discovered from PS1 and three sources from the literature (PSO 006+39, PSO 338+29, and HSC 1205). These observations have been obtained with a variety of telescopes and spectrographs: VLT/FORS2, P200/DBSP, MMT/Red Channel, Magellan/FIRE, VLT/X-Shooter (Vernet et al. 2011), Keck/LRIS (Oke et al. 1995; Rockosi et al. 2010), and GNT/GNIRS (Dubbeldam et al. 2000). We take the remaining spectroscopic data from the literature. The details (i.e., observing dates, instruments, telescopes, exposure times, and references) for all the spectra presented here are reported in Table 2. In case of multiple observations of one object, we use the weighted mean of the spectra. We scale the spectra to the observed J-band magnitudes (see Table 3), with the exceptions of PSO 006+39, for which we do not have this information, and PSO 011+09 and PSO 261+19, which only have optical coverage; in these cases, we normalize the spectra to the y_{P1} magnitudes. We also correct the data for Galactic extinction, using the extinction law provided by Calzetti et al. (2000). The reduced spectra are shown in Figure 3.

3.3. NOEMA Observations

Four quasars in our sample (PSO 323+12, PSO 338+29, PSO 006+39, and HSC 1205) have been observed with the NOrthern Extended Millimeter Array (NOEMA): these data, together with the ones retrieved from the literature (Venemans et al. 2012, 2016; Bañados et al. 2015b; R. Decarli et al., in preparation; see also Table 5 and Section 5.1), complete coverage of the [C II] 158 μm emission line for all currently published $z \geqslant 6.5$ quasars. The NOEMA observations were carried out in the compact array configuration, for which the primary beam at 250 GHz is $\sim 20''$ (full width at half power). Data were processed with the latest release of the software clic in the GILDAS suite and analyzed using the software mapping, together with a number of custom routines written by our group.

[21] http://www.lco.cl/telescopes-information/irenee-du-pont/instruments/website/retrocam

[22] http://www.caha.es/CAHA/Instruments/CAFOS/index.html

Table 1
Imaging Follow-up Observation Campaigns for PS1 High-redshift Quasar Candidates

Date	Telescope/Instrument	Filters	Exposure Time
2014 May 9	CAHA 3.5 m/Omega2000	z_{O2K}, Y_{O2K}, J_{O2K}	300 s
2014 Jul 23–27	NTT/EFOSC2	I_E, Z_E	600 s
2014 Jul 25	NTT/SofI	J_S	600 s
2014 Aug 7 and 11–13	CAHA 3.5 m/Omega2000	Y_{O2K}, J_{O2K}	600 s
2014 Aug 22–24	CAHA 2.5 m/CAFOS	i_w	1800 s
2015 Feb 22	NTT/SofI	J_S	300 s
2016 Jun 5–13	MPG 2.2 m/GROND	g_G, r_G, i_G, z_G, J_G, H_G, K_G	1440 s
2016 Sep 11–13	NTT/EFOSC2	I_E	900 s
2016 Sep 16–25	MPG 2.2 m/GROND	g_G, r_G, i_G, z_G, J_G, H_G, K_G	1440 s
2016 Sep 18–21	du Pont/Retrocam	Y_{retro}	1200 s

PSO 323+12 was observed in a Director's Discretionary Time program (project ID: E15AD) on 2015 December 28, with seven 15 m antennae arranged in the 7D configuration. The source MWC 349 was used for flux calibration, while the quasar 2145+067 was used for phase and amplitude calibration. The system temperature was in the range 110–160 K. Observations were performed with average precipitable water vapor conditions (~2.2 mm). The final cube includes 5159 visibilities, corresponding to 3.07 hr on source (seven antennas equivalent). After collapsing the entire 3.6 GHz bandwidth, the continuum rms is 0.146 mJy beam^{-1}.

PSO 338+29 was observed on 2015 December 3 (project ID: W15FD) in the 7C array configuration. MWC 349 was observed for flux calibration, while the quasar 2234+282 was targeted for phase and amplitude calibration. The typical system temperature was 85–115 K. Observations were carried out in good water vapor conditions (1.7–2.0 mm). The final data cube consists of 4110 visibilities, corresponding to 2.45 hr on source (seven-antenna equivalent). The synthesized beam is $1\farcs35 \times 0\farcs69$. The rms of the collapsed data cube is 0.215 mJy beam^{-1}.

PSO 006+39 was observed in two visits, on 2016 May 20 and 2016 July 7, as part of the project S16CO, with five to seven antennae. The May visit was hampered by high precipitable water vapor (~3 mm), yielding high system temperature (200–300 K). The July track was observed in much better conditions, with precipitable water vapor (pwv) ~1.3 mm and T_{sys} = 105–130 K. The final cube consists of 2700 visibilities, corresponding to 2.25 hr on source (six-antenna equivalent), with a continuum sensitivity of 0.178 mJy beam^{-1}. The synthesized beam is $1\farcs19 \times 0\farcs61$.

HSC 1205 was also observed as part of project S16CO, on 2016 October 29, using the full eight-antenna array. MWC 349 was observed for flux calibration, while the quasar 1055+018 served as phase and amplitude calibrator. The precipitable water vapor was low (~1.3 mm), and the system temperature was 120–180 K. The final cube consists of 2489 visibilities, or 1.11 hr on source (eight-antenna equivalent). The synthesized beam is $1\farcs19 \times 0\farcs61$, and the continuum rms is 0.176 mJy beam^{-1}.

4. Individual Notes on Six New Quasars from PS1

We present six new quasars at $z \sim 6.5$ discovered from the PS1 survey; here we present a brief observational summary of each source.

4.1. PSO J011.3899+09.0325 at $z = 6.42$

Follow-up imaging data for PSO 011+09 were acquired with MPG 2.2 m/GROND and du Pont/Retrocam in 2016 September; its quasar nature was confirmed with a short 600 s low-resolution prism mode spectrum using Magellan/FIRE on 2016 November 20. We then obtained a higher-S/N, higher-resolution optical spectrum with Keck/LRIS. We consider in this work only the latter spectroscopic observation (see Figure 3) because the FIRE spectrum has a very limited S/N and overexposed H and K bands. It is a relatively faint object, with $J_G = 20.8$, and presents a very flat $Y_{retro} - J_G$ color of 0.01 (see Table 4). This quasar does not show strong emission lines. Through a comparison with SDSS quasar templates (see Section 5.1), we calculate a redshift of $z = 6.42$, with an uncertainty of $\Delta z = 0.05$.

4.2. PSO J183.1124+05.0926 at $z = 6.4386$

PSO 183+05 was first followed up with the SofI and EFOSC2 instruments at the NTT, in 2015 February. The discovery spectrum was taken with the Red Channel spectrograph at the MMT; higher-quality spectra were later acquired with Magellan/FIRE and VLT/FORS2, in 2015 April and May, respectively. Evidence was found for the presence of a very proximate damped Lyman absorber (DLA; $z \sim 6.404$) along the same line of sight (see also Chen et al. 2016). An in-depth study of this source will be presented in E. Bañados et al. (in preparation).

4.3. PSO J231.6576–20.8335 at $z = 6.5864$

The imaging follow-up for PSO 231-20 was also undertaken with EFOSC2 and SofI at the NTT in 2015 February. It was spectroscopically confirmed with Magellan/FIRE on 2015 March 13, and we acquired a VLT/FORS2 spectrum on 2015 May 15. With a J-band magnitude of 19.66, this quasar is the brightest newly discovered object, and one of the brightest known at $z > 6.5$, alongside PSO 036+03 and VDES J0224–4711.

4.4. PSO J247.2970+24.1277 at $z = 6.476$

We acquired follow-up photometric observations of PSO 247+24 with CAFOS and Omega2000 at the 2.2 m and 3.5 m telescopes at CAHA, respectively. We confirmed its quasar nature with VLT/FORS2 in 2016 March, and we obtained NIR spectroscopy with Magellan/FIRE in the same month. This quasar presents prominent broad emission lines (see Figure 3).

Table 2
Spectroscopic Observations of the $z \gtrsim 6.5$ Quasars Presented in This Study

Object	Date	Telescope/Instrument	λ Range (μm)	Exposure Time (s)	Slit Width	Reference
PSO J006.1240+39.2219	2016 Jul 5	Keck/LRIS	0.55–1.1	1800	1.″0	(6)
PSO J011.3899+09.0325	2016 Nov 20	Magellan/FIRE	0.82–2.49	600	1.″0	(6)
	2016 Nov 26	Keck/LRIS	0.55–1.1	900	1.″0	(5)
VIK J0109–3047	2011 Aug–Nov	VLT/X-Shooter	0.56–2.48	21,600	0.″9–1.″5	(1), (2)
PSO J036.5078+03.0498	2015 Dec 22–29	VLT/FORS2	0.74–1.07	4000.0	1.″0	(5)
	2014 Sep 4–6	Magellan/FIRE	0.82–2.49	8433	0.″6	(3)
VIK J0305–3150	2011 Nov–2012 Jan	Magellan/FIRE	0.82–2.49	26,400	0.″6	(1), (2)
PSO J167.6415–13.4960	2014 Apr 26	VLT/FORS2	0.74–1.07	2630	1.″3	(3)
	2014 May 30–Jun 2	Magellan/FIRE	0.82–2.49	12,004	0.″6	(3)
ULAS J1120+0641	2011	GNT/GNIRS	0.90–2.48		1.″0	(5)
HSC J1205–0000	2016 Mar 14	Magellan/FIRE	0.82–2.49	14456	0.″6	(6)
PSO J183.1124+05.0926	2015 May 8	VLT/FORS2	0.74–1.07	2550	1.″3	(6)
	2015 Apr 6	Magellan/FIRE	0.82–2.49	11730	0.″6	(4), (5)
PSO J231.6576–20.8335	2015 May 15	VLT/FORS2	0.74–1.07	2600	1.″3	(6)
	2015 Mar 13	Magellan/FIRE	0.82–2.49	9638	0.″6	(4), (5)
PSO J247.2970+24.1277	2016 Mar 10	VLT/FORS2	0.74–1.07	1500	1.″0	(6)
	2016 Mar 31	Magellan/FIRE	0.82–2.49	6626	0.″6	(4), (6)
PSO J261.0364+19.0286	2016 Sep 12	P200/DBSP	0.55–1.0	3600	1.″5	(6)
PSO J323.1382+12.2986	2015 Nov 5	VLT/FORS2	0.74–1.07	1500	1.″0	(6)
	2016 Aug 15	Magellan/FIRE	0.82–2.49	3614	0.″6	(6)
PSO J338.2298+29.5089	2014 Oct 19	MMT/Red Channel	0.67–1.03	1800	1.″0	(3)
	2014 Oct 30	Magellan/FIRE	0.82–2.49	7200	0.″6	(3)
	2014 Nov 27	LBT/MODS	0.51–1.06	2700	1.″2	(3)
VIK J2348–3054	2011 Aug 19–21	VLT/X-Shooter	0.56–2.48	8783	0.″9–1.″5	(1), (2)

Note. We present optical/NIR spectra for all the newly discovered objects and for some known sources. We also gather data from the literature. References: (1) Venemans et al. 2013; (2) De Rosa et al. 2014; (3) Venemans et al. 2015a; (4) Chen et al. 2016; (5) Mortlock et al. 2011; and (6) this work.

4.5. PSO J261.0364+19.0286 at $z = 6.44$

We used the 2.2 m MPG/GROND and SofI at the NTT in 2016 June–September to acquire follow-up photometry for PSO 261+19. Spectroscopic observations with the DBSP at the Palomar Observatory in 2016 September confirmed that the object is a quasar at $z = 6.44 \pm 0.05$ (redshift from SDSS quasar template fitting; see Section 5.1). Similar to PSO 11 +09, this is a relatively faint quasar, with $J_G = 21.09$.

4.6. PSO J323.1382+12.2986 at $z = 6.5881$

Imaging follow-up of PSO 323+12 was acquired with CAHA 3.5 m/Omega2000 and NTT/SofI in 2014 August and 2015 February, respectively. Spectroscopic observations with FORS2 at the VLT in 2015 December confirmed that the source is a high-redshift quasar. The NIR spectrum was later obtained with Magellan/FIRE, in 2016 August. This quasar is the one at the highest redshift among the newly discovered objects ($z = 6.5881$; see Section 5.1).

5. Analysis

We next present a comprehensive study of the quasar population at the highest redshifts currently known ($z \gtrsim 6.42$). We consider a total sample of 15 quasars, 6 newly presented here and discovered in our search in the PS1 catalog (see Sections 2 and 3) and 9 sources from the literature (one from UKIDSS, three from VIKING, four from PS1, and one from HSC). We report their coordinates, redshifts, and discovery references in Table 5. Due to the variety of the data collected (e.g., we do not have NIR spectra or [C II] observations for all the objects in this work), we consider different subsamples of quasars in the following sections, depending on the physical parameters that we could measure.

5.1. Redshifts

An accurate measurement of high-redshift quasar systemic redshifts is challenging. Several techniques have been implemented, and previous studies have shown that redshift values obtained with different indicators often present large scatters or substantial shifts (e.g., De Rosa et al. 2014; Venemans et al. 2016). In general, the most precise redshift indicators (with measurement uncertainties of $\Delta z < 0.004$) are the atomic or molecular narrow emission lines, originating from the interstellar medium of the quasar host galaxy. This emission, in particular the [C II] lines, and the underlying dust continuum emission are observable in the millimeter wavelength range at $z \sim 6$. When available, we adopt $z_{[C\,II]}$ measurements for the objects in our sample (11 out of 15). We take advantage of our new NOEMA observations of four quasars (see Section 3.3) to estimate their systemic redshifts from the [C II] 158 μm emission line. A flat continuum and a Gaussian profile are fitted to the spectra, as shown in Figure 4, allowing us to derive $z_{[C\,II]}$ for PSO 006+39, PSO 323+12, and PSO 338+29. The frequency of the observations of HSC 1205 was tuned for a redshift of $z = 6.85$, in the range of redshifts originally reported in the discovery paper (Matsuoka et al. 2016). No [C II] emission line is detected from the quasar, possibly due to our frequency tuning not being centered on the true redshift of the source. This scenario is supported by our own new NIR observations of the Mg II line, which place HSC 1205 at $z = 6.73 \pm 0.02$ (see below, Table 5 and Section 5.5); this is also consistent with the new redshift reported in

Table 3
PS1 PV3, $z_{\rm decam}$, J, and *WISE* Photometry and Galactic $E(B-V)$ Values (from Schlegel et al. 1998) of the Quasars Analyzed Here

Name	$z_{\rm P1}$	$y_{\rm P1}$	$z_{\rm decam}$	J	$J_{\rm ref}$	$W1$	$W2$	$E(B-V)$
PSO J006.1240+39.2219	>23.02	20.06 ± 0.07	···	···	···	···	···	0.075
PSO J011.3899+09.0325	>22.33	20.60 ± 0.09	···	20.80 ± 0.13	(6)	20.19 ± 0.19	···	0.059
VIK J0109–3047	···	···	···	21.27 ± 0.16	(3)	20.96 ± 0.32	···	0.022
PSO J036.5078+03.0498	21.48 ± 0.12	19.30 ± 0.03	20.01 ± 0.01	19.51 ± 0.03	(4)	19.52 ± 0.06	19.69 ± 0.14	0.035
VIK J0305–3150	···	···	···	20.68 ± 0.07	(3)	20.38 ± 0.14	20.09 ± 0.24	0.012
PSO 167.6415–13.4960	>22.94	20.55 ± 0.11	···	21.21 ± 0.09	(4)	···	···	0.057
ULAS J1120+0641[a]	>23.06	20.76 ± 0.19	22.38 ± 0.1	20.34 ± 0.15	(1)	19.81 ± 0.09	19.96 ± 0.23	0.052
HSC J1205–0000[b]	>22.47	>21.48	···	21.95 ± 0.21	(5)	19.98 ± 0.15	19.65 ± 0.23	0.0243
PSO J183.1124+05.0926	21.68 ± 0.10	20.01 ± 0.06	20.53 ± 0.02	19.77 ± 0.08	(6)	19.74 ± 0.08	20.03 ± 0.24	0.0173
PSO J231.6576–20.8335	>22.77	20.14 ± 0.08	···	19.66 ± 0.05	(6)	19.91 ± 0.15	19.97 ± 0.35	0.133
PSO J247.2970+24.1277	>22.77	20.04 ± 0.07	20.82 ± 0.03	20.23 ± 0.09	(6)	19.46 ± 0.04	19.28 ± 0.08	0.053
PSO J261.0364+19.0286	>22.92	20.98 ± 0.13	···	21.09 ± 0.18	(6)	20.61 ± 0.21	···	0.045
PSO J323.1382+12.2986	21.56 ± 0.10	19.28 ± 0.03	···	19.74 ± 0.03	(6)	19.06 ± 0.07	18.97 ± 0.12	0.108
PSO J338.2298+29.5089	>22.63	20.34 ± 0.1	21.15 ± 0.05	20.74 ± 0.09	(4)	20.51 ± 0.14	···	0.096
VIK J2348–3054	···	···	···	21.14 ± 0.08	(3)	20.36 ± 0.17	···	0.013

Notes. The limits are at 3σ significance. The J-band information is from (1) UKIDSS, (2) VHS, (3) Venemans et al. (2013), (4) Venemans et al. (2015a), (5) Matsuoka et al. (2016), and (6) this work (in case we have follow-up photometry on the quasar, we report the magnitude with the best S/N; see also Table 4). The $z_{\rm decam}$ information is taken from the last DECaLS DR3 release. The *WISE* data are from ALLWISE or, in case the object was present in DECaLS DR3, from the UNWISE catalog (Lang 2014; Meisner et al. 2016).

[a] The PS1 magnitudes are taken from the PV2 catalog, since the object is not detected in PV3, having S/N < 5 in all bands. However, forced photometry on the $y_{\rm P1}$ PV3 stack image at the quasar position reveals a faint source with S/N = 4.3 in PV3.

[b] This object does not appear in the PS1 PV3 catalog. The PS1 magnitudes are obtained by performing forced photometry on the $z_{\rm P1}$ and $y_{\rm P1}$ PV3 images.

Matsuoka et al. (2017; $z = 6.75$). At this redshift, the [C II] emission line falls at an observed frequency of 245.87 GHz, outside the range probed in the NOEMA data (see top panel of Figure 4). The redshifts of PSO 231-20, PSO 167-13, and PSO 183+05 are measured from the [C II] line, observed in our ALMA survey of cool gas and dust in $z \gtrsim 6$ quasars (R. Decarli et al., in preparation). We take the values of $z_{\rm [C\,II]}$ for ULAS 1120, VIK 2348, VIK 0109, VIK 0305, and PSO 036+03 from the literature (Venemans et al. 2012, 2016; Bañados et al. 2015b).

The second-best way to estimate redshifts is through the low-ionization MG II λ2798.75 broad emission line, which is observable in the K band at $z > 6$. This radiation is emitted from the broad-line region (BLR), and therefore it provides a less precise measurement than the narrow emission from the cool gas traced by the [C II] emission. Several studies, based on $z < 1$ quasar samples, demonstrated that MG II emission is a far more reliable redshift estimator than other high-ionization emission lines (e.g., C IV λ1549.06 and Si IV λ1396.76), and it has a median shift of only 97 ± 269 km s^{-1} with respect to the narrow [O III] λ5008.24 emission line (Richards et al. 2002). We provide $z_{\rm Mg\,II}$ for HSC 1205 and PSO 247+24, for which we have no [C II] observations, as their best redshift estimates. We also calculate $z_{\rm Mg\,II}$ for the remaining nine quasars in our sample with NIR spectra (see Section 5.5 and Table 7). Our new values are consistent, within 1σ uncertainties, with the measurements from the literature for ULAS 1120, VIK 2348, VIK 0109, and VIK 0305 (De Rosa et al. 2014) and for PSO 036+03, PSO 167-13, and PSO 338+29 (Venemans et al. 2015a). However, it has been recently shown that, at $z \gtrsim 6$, the mean and standard deviation of the shifts between $z_{\rm Mg\,II}$ and the quasar systemic redshift (as derived from the [C II] emission line) are significantly larger (480 ± 630 km s^{-1}) than what is found at low redshift (see Venemans et al. 2016). We can study the distribution of the shifts between the redshifts measured from MG II and [C II] (or CO) emission lines, considering both the newly discovered and/or newly analyzed sources in this sample and quasars at $z \gtrsim 6$ with such information from the literature (six objects; the values of $z_{\rm Mg\,II}$ are taken from Willott et al. 2010a; De Rosa et al. 2011, while the $z_{\rm [C\,II]}$ measurements are from Carilli et al. 2010; Wang et al. 2011; Willott et al. 2013, 2015). The distribution of the shifts is shown in Figure 5. They span a large range of values, from +2300 to −265 km s^{-1}. We obtain a mean and median of 485 and 270 km s^{-1}, respectively, and a large standard deviation of 717 km s^{-1}. These results are in line with what was found by Venemans et al. (2016), although we measure a less extreme median value (270 km s^{-1} against 467 km s^{-1}) and confirm that the MG II emission line can be significantly blueshifted with respect to the [C II] emission in high-redshift quasars. This effect is unlikely to be due to the infalling of [C II] in the quasars' host galaxies: resolved observations of the [C II] emission line in high-redshift quasars show that the gas is often displaced in a rotating disk (e.g., Wang et al. 2013; Shao et al. 2017), and no evidence is found in our sample to point at a different scenario. Also, the gas free-fall time would be too short (∼few Myr, considering a typical galactic size of ∼2 kpc and gas mass of $\sim 10^8\,M_\odot$; e.g., Venemans et al. 2016) to allow the ubiquitous observation of [C II] in quasars at these redshifts. An alternative scenario explaining the detected blueshifts would be that the BLRs in these quasars are characterized by strong outflows/wind components.

Finally, for PSO 261+19 and PSO 011+09, only the optical spectra are available. We derive their redshifts from a χ^2 minimization technique, comparing their spectrum with the low-redshift quasar template from Selsing et al. (2016) and the composite of $z \sim 6$ quasars presented by Fan et al. (2006); for further details on this procedure see Bañados et al. (2016). The redshift measurements obtained in this case are the most uncertain, with $\Delta z = 0.05$. We report all the redshifts, their uncertainties, the different adopted techniques, and references in Table 5.

Table 4
Photometry from Our Follow-up Campaigns for the Newly Discovered PS1 Quasars

Name	
PSO J011.3899+09.0325	$i_G > 23.36$; $z_G = 22.38 \pm 0.16$; $Y_{retro} = 20.81 \pm 0.07$; $J_G = 20.80 \pm 0.13$
PSO J183.1124+05.0926	$I_E = 23.51 \pm 0.21$; $Z_E = 20.93 \pm 0.09$; $J_S = 19.77 \pm 0.08$
PSO J231.6576–20.8335	$I_E > 23.81$; $J_S = 19.66 \pm 0.05$
PSO J247.2970+24.1277	$i_w > 22.36$; $i_{MMT} > 22.69$; $z_{O2k} = 20.89 \pm 0.07$; $Y_{O2k} = 20.04 \pm 0.24$; $J_{O2k} = 20.23 \pm 0.09$
PSO J261.0364+19.0286	$i_G > 23.40$; $I_E > 24.01$; $z_G = 22.18 \pm 0.12$; $J_G = 21.09 \pm 0.18$; $H_G = 20.92 \pm 0.30$
PSO J323.1382+12.2986	$z_{O2k} = 20.14 \pm 0.05$; Y_{O2k}=19.45 $\pm$ 0.07; $J_S = 19.74 \pm 0.03$

Note. The limits are at 3σ. See also Table 1.

5.2. Absolute Magnitude at 1450 Å

The apparent magnitude at rest-frame wavelength 1450 Å (m_{1450}) is a quantity commonly used in characterizing quasars. Following Bañados et al. (2016), we extrapolate m_{1450} from the J-band magnitude, assuming a power-law fit of the continuum ($f \sim \lambda^{-\alpha}$), with $\alpha = -1.7$ (Selsing et al. 2016).[23] We derive the corresponding absolute magnitude (M_{1450}) using the redshifts reported in Table 5. In Figure 6 we show the distribution of M_{1450}, a proxy of the rest-frame UV luminosity of the quasars, as a function of redshift for the sources in our sample and a compilation of quasars at $5.5 \lesssim z \lesssim 6.4$ (see references in Bañados et al. 2016, Table 7). The highest-redshift objects considered here show similar luminosities to the ones at $z \sim 6$. In Table 6 we report the values of m_{1450} and M_{1450} for the quasars analyzed here.

5.3. Quasar Continuum

The UV/optical rest-frame quasar continuum emission results from the superposition of multiple components: the nonthermal, power-law emission from the accretion disk; the stellar continuum from the host galaxy; the Balmer pseudo-continuum; and the pseudo-continuum due to the blending of several broad Fe II and Fe III emission lines. In the literature, the continua of very luminous quasars such as the ones studied here have been generally reproduced with a simple power law, since the host galaxy emission is outshined by the radiation from the central engine. Here, we first model the continuum with a single power law:

$$F_\lambda = F_0 \left(\frac{\lambda}{2500\text{Å}} \right)^\alpha. \quad (8)$$

We consider regions of the rest-frame spectra that are free from strong emission lines: [1285–1295; 1315–1325; 1340–1375; 1425–1470; 1680–1710; 1975–2050; 2150–2250; and 2950–2990] Å (Decarli et al. 2010). We slightly adjust these windows to take into account sky absorption, residual sky emission, and regions with low S/N. We use a χ^2 minimization technique to derive the best values and corresponding uncertainties for α and F_0 (see Table 6).

Vanden Berk et al. (2001) and Selsing et al. (2016) report typical slopes of $\alpha = -1.5$ and -1.7, respectively, for composite templates of lower-redshift ($z \sim 2$) SDSS quasars. In our case, we find that α may significantly vary from object to object, with a mean of $\alpha = -1.6$ and a 1σ dispersion of 1.0. This large range of values is in agreement with previous studies of lower-redshift quasars ($z < 3$, Decarli et al. 2010; $4 \lesssim z \lesssim 6.4$, De Rosa et al. 2011, 2014). However, we notice that the quasars for which we only have optical spectral information are poorly reproduced by a power-law model, and the slopes obtained are characterized by large uncertainties (see Table 6). If we consider only the objects with NIR spectroscopy, we obtain a mean slope of $\alpha = -1.2$, with a 1σ scatter of 0.4.

We use these power-law continuum fits in the modeling of the C IV broad emission line in our quasars with NIR coverage (see Section 5.4). Afterward, we implement a more accurate modeling of the spectral region around the Mg II emission line, which, together with the Fe II emission and the rest-frame UV luminosity, is a key tool commonly used to derive crucial quasar properties, e.g., black hole masses (see Section 5.6).

5.4. C IV Blueshifts

The peaks of high-ionization, broad emission lines, such as C IV, show significant shifts blueward with respect to the systemic redshifts in quasars at low redshift (e.g., Richards et al. 2002): this has been considered a signature of outflows and/or of an important wind component in quasars BLRs (e.g., Leighly 2004). Hints have been found of even more extreme blueshifts at high redshifts (e.g., De Rosa et al. 2014).

Here we investigate the presence of C IV shifts in our high-redshift quasars by modeling the emission line with a single Gaussian function, after subtracting the continuum power-law model obtained in Section 5.3 from the observed spectra. We report the computed C IV shifts with respect to the Mg II emission line (see Section 5.1 and Table 7) in Table 6. We consider here the Mg II and not the [C II] line since we want to consistently compare our high-redshift sources to $z \sim 1$ quasars (see below), for which the [C II] measurements are not always available. We adopt a positive sign for blueshifts. All quasars in our sample show significant blueshifts, from ~730 to ~5900 km s^{-1}. For the previously studied case of ULAS 1120, the value found here is consistent with the ones reported in the literature (De Rosa et al. 2014; Greig et al. 2017). We neglect the following here: PSO 167-13 and HSC 1205, due to the low S/N; PSO 183+05, for which we do not have a measurement of the Mg II redshift (see Section 5.5); and PSO 011+09, PSO 006+39, and PSO 261+19, since we do not have NIR spectral coverage (see Section 3 and Figure 3); also, we still consider VIK2348, but with the caveat that this object was flagged as a possible broad absorption line (BAL) quasar (De Rosa et al. 2014). In Figure 7 we show the distribution of the blueshifts for high-redshift quasars in this work (bottom panel) and for a sample of objects at lower redshift taken from the SDSS DR7 catalog (Shen et al. 2011; top panel). For comparison, we select a subsample of objects at low redshift, partially following Richards et al. (2011): we consider quasars in the redshift range

[23] For PSO 006+39 we use the y_{P1}-band magnitude, since we do not have J-band information.

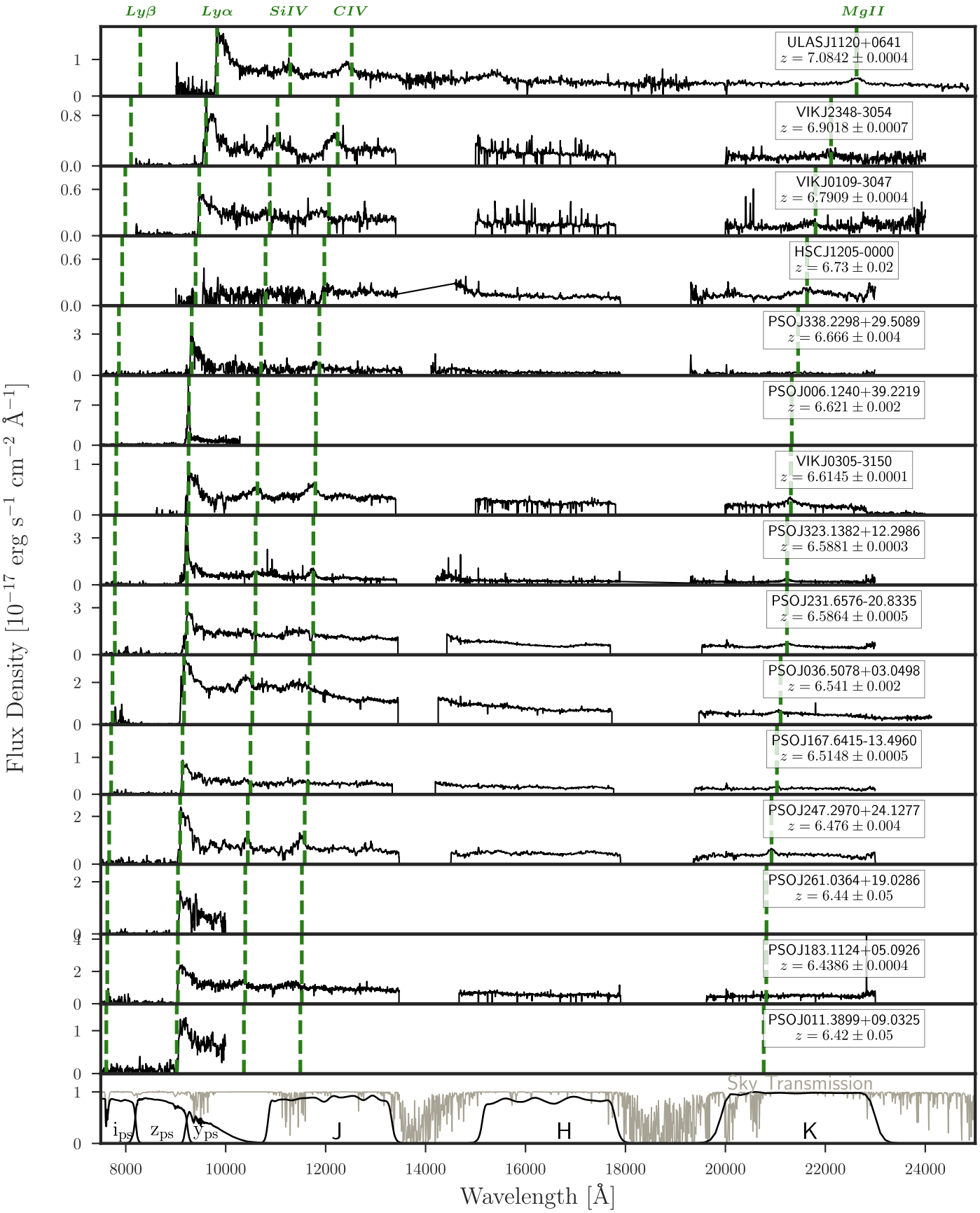

Figure 3. Binned spectra of the 15 $z \gtrsim 6.5$ quasars in the sample considered here. The quasars PSO 323+12, PSO 231-20, PSO 247+24, PSO 011+09, PSO 261+19, and PSO 183+05 are newly discovered from the PS1 PV3 survey; the other objects are taken from the literature (see Table 5). The locations of key emission lines (Lyβ, Lyα, Si IV, C IV, and Mg II) are highlighted with dashed green lines.

Table 5
Sample of Quasars at $z \gtrsim 6.42$ Considered in This Study

Name	R.A.(J2000)	Decl. (J2000)	z	$z_{\rm err}$	z Method	Ref. Discovery	Ref. z
PSO J006.1240+39.2219	00:24:29.772	+39:13:18.98	6.621	0.002	[C II]	(5)	(6)
PSO J011.3899+09.0325	00:45:33.568	+09:01:56.96	6.42	0.05	template	(6)	(6)
VIK J0109–3047	01:09:53.131	−30:47:26.32	6.7909	0.0004	[C II]	(2)	(8)
PSO J036.5078+03.0498	02:26:01.876	+03:02:59.39	6.541	0.002	[C II]	(3)	(9)
VIK J0305–3150	03:05:16.916	−31:50:55.90	6.6145	0.0001	[C II]	(2)	(8)
PSO J167.6415–13.4960	11:10:33.976	−13:29:45.60	6.5148	0.0005	[C II]	(3)	(10)
ULAS J1120+0641	11:20:01.479	+06:41:24.30	7.0842	0.0004	[C II]	(1)	(7)
HSC J1205–0000	12:05:05.098	−00:00:27.97	6.73	0.02	Mg II	(4)	(6)
PSO J183.1124+05.0926	12:12:26.981	+05:05:33.49	6.4386	0.0004	[C II]	(6)	(10)
PSO J231.6576–20.8335	15:26:37.841	−20:50:00.66	6.5864	0.0005	[C II]	(6)	(10)
PSO J247.2970+24.1277	16:29:11.296	+24:07:39.74	6.476	0.004	Mg II	(6)	(6)
PSO J261.0364+19.0286	17:24:08.743	+19:01:43.12	6.44	0.05	template	(6)	(6)
PSO J323.1382+12.2986	21:32:33.191	+12:17:55.26	6.5881	0.0003	[C II]	(6)	(6)
PSO J338.2298+29.5089	22:32:55.150	+29:30:32.23	6.666	0.004	[C II]	(3)	(6)
VIK J2348–3054	23:48:33.334	−30:54:10.24	6.9018	0.0007	[C II]	(2)	(8)

Note. The objects were discovered by several studies: (1) Mortlock et al. 2011; (2) Venemans et al. 2013; (3) Venemans et al. 2015a; (4) Matsuoka et al. 2016; (5) Tang et al. 2017; (6) this work. In addition to this work (6), the redshifts measurements are taken from the following: (7) Venemans et al. 2012; (8) Venemans et al. 2016; (9) Bañados et al. 2015b; (10) R. Decarli et al., in preparation.

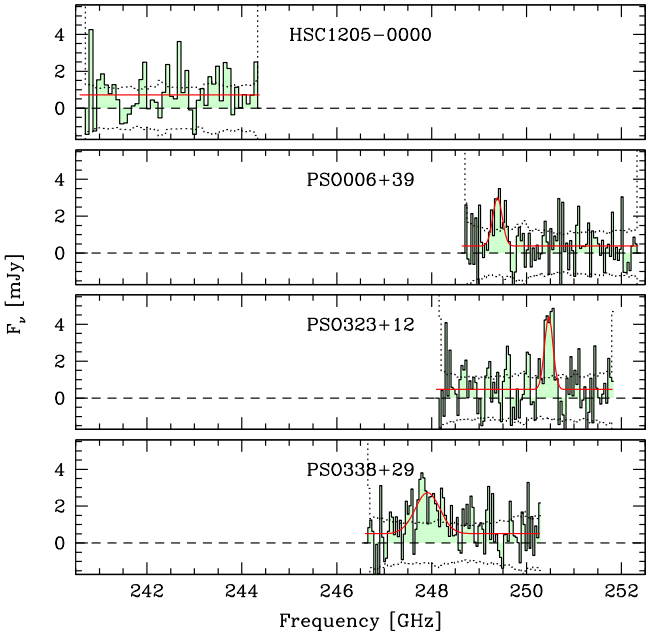

Figure 4. NOEMA 1.2 mm observations of the [C II] 158 μm emission line and underlying dust continuum for four objects in our sample. The extracted spectra are fitted with a flat continuum and Gaussian function. We detect [C II] 158 μm emission for all the objects except HSC 1205, whose observations were tuned based on the initial redshift range reported by Matsuoka et al. (2016): our Mg II emission line detection, consistent with the new redshift in Matsuoka et al. (2017), positions its [C II] emission line out of the covered band (see text for details). We still detect the dust continuum from this quasar.

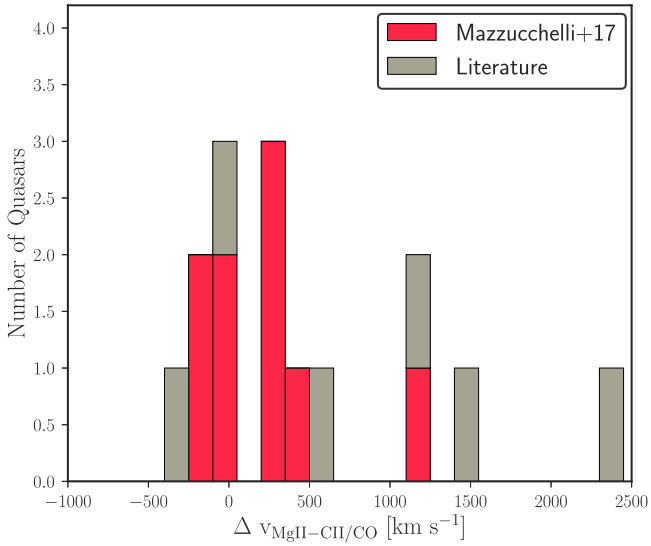

Figure 5. Difference between the velocity measurements obtained from MG II and [C II] or CO emission lines for a sample of $z \gtrsim 6$ quasars. We consider nine objects in this work for which we have both measurements (red histogram; see Tables 5 and 7) and six quasars from the literature (gray histogram; see text for references). The positive sign indicates the blueshift of the Mg II emission line. The offsets span a large range of values, with a mean and standard deviation of 485 ± 717 km s^{-1}, consistent with the results obtained by Venemans et al. (2016).

$1.52 < z < 2.2$ (where both the C IV and Mg II emission lines are covered), with significant detection of the broad C IV emission line (FWH $M_{\rm C\,IV} > 1000$ km s^{-1}, FWH $M_{\rm C\,IV} > 2\sigma_{\rm FWHM_{C\,IV}}$, EW$_{\rm C\,IV} > 5$ Å, EW$_{\rm C\,IV} > 2\sigma_{\rm EW_{C\,IV}}$, where $\sigma_{\rm FWHM}$ and $\sigma_{\rm EW}$ are the uncertainties on the FWHM and EW, respectively) and of the Mg II emission line (FWH $M_{\rm Mg\,II} > 1000$ km s^{-1}, FWH $M_{\rm Mg\,II} > 2\sigma_{\rm FWHM_{Mg\,II}}$, EW$_{\rm Mg\,II} > 2\sigma_{\rm EW_{Mg\,II}}$), and those that are not flagged as BAL quasars (BAL FLAG = 0). The total number of objects is ∼22,700; the mean, median, and standard deviation of the C IV blueshift with respect to the Mg II emission line in this lower-redshift sample are 685, 640, and 871 km s^{-1}, respectively. If we consider a subsample of the brightest quasars (with luminosity at rest-frame wavelength 1350 ÅŁ$_{\lambda,1350} > 3 \times 10^{46}$ erg s^{-1}; 1453 objects), we recover higher mean and median values (994 and 930 km s^{-1}, respectively), but with large scatter (see Figure 7). We also draw a subsample of SDSS quasars matched to the $L_{\lambda,1350}$ distribution of the high-redshift sample (for details on the method, see Section 5.6). In this case, the mean and median values of the C IV blueshift are 790 and 732 km s^{-1}, respectively, with a standard deviation of 926 km s^{-1}. The high-redshift quasar population is characterized by a mean,

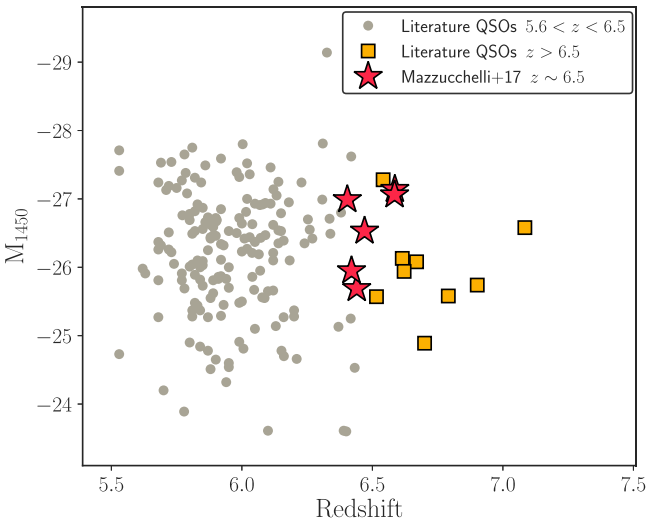

Figure 6. Absolute magnitude at rest-frame wavelength 1450 Å, M_{1450}, against redshift, for quasars at $5.5 \lesssim z \lesssim 6.4$ from the literature (gray circles; see Bañados et al. 2016, Table 7, for references) and in the sample considered here, at $z \gtrsim 6.42$, both taken from the literature (for references see Table 5; yellow squares) and newly discovered in this work (red stars). All the M_{1450} values were derived with a consistent methodology (see text). The magnitudes of the quasars presented here span a similar range to the ones at lower redshifts.

median, and standard deviation of 2940, 2438, and 1761 km s^{-1}; C IV blueshifts tend to be much higher at high redshift, as already observed for the Mg II shifts with respect to the systemic quasar redshifts traced by CO/[C II] emission (see Section 5.1 and Figure 5).

In Table 6 we report the values of C IV rest-frame EW of the quasars in the sample of this work, which are plotted as a function of C IV blueshifts, together with objects at low redshift, in Figure 8. Richards et al. (2011) show that C IV blueshifts correlate with C IV EW at $z \sim 1$–2: quasars with large EW are characterized by small blueshifts, while objects with small EW present both large and small blueshifts; no objects were found with strong C IV line and high blueshift. The high-redshift quasars studied here follow the trend of the low-redshift objects, with extreme C IV blueshifts and EW equal to or lower than the bulk of the SDSS sample. This is also in line with the higher fraction of weak emission line (WEL) quasars found at high redshifts (e.g., Bañados et al. 2014, 2016).

However, we note that C IV blueshifts scale with quasar UV luminosities: this is linked to the anticorrelation between luminosity and emission line EW (i.e., Baldwin effect; e.g., Baldwin 1977; Richards et al. 2011). Also, the $z \gtrsim 6.5$ quasars presented here are biased toward higher luminosities (e.g., due to our selection criteria): we may then be considering here only the extreme cases of the highest-redshift quasar population, and therefore missing the objects at lower luminosity and lower C IV blueshifts.

5.5. Mg II and Fe II Emission Modeling

We fit the quasar emission, in the rest-frame wavelength window $2100 < \lambda/\text{Å} < 3200$, as a superposition of multiple components:

1. the quasar nuclear continuum emission, modeled as a power law (see Equation (8));
2. the Balmer pseudo-continuum, modeled with the function provided by Grandi (1982; see their Equation (7)) and imposing that the value of the flux at $\lambda_{\rm rf} = 3675$ Å is equal to 10% of the power-law continuum contribution at the same wavelength;
3. the pseudo-continuum Fe II emission, for which we use the empirical template by Vestergaard & Wilkes (2001); and
4. the Mg II emission line, fitted with a single Gaussian function.

We use a χ^2 minimization routine to find the best-fitting parameters (slope and normalization) for the nuclear emission, together with the best scaling factor for the iron template; once we have subtracted the best continuum model from the observed spectra, we fit the Mg II emission line (for further details see Decarli et al. 2010). We apply this routine to all the quasars with NIR information in our sample. We exclude PSO 183+05 from this analysis, since this source is a weak emission line quasar (see Figure 3) and the Mg II fit is highly uncertain. We show the obtained fit for the 11 remaining objects in Figure 9. In Table 7, we list the derived monochromatic luminosities at rest-frame $\lambda_{\rm rf} = 3000$Å(λL_{3000}), calculated from the continuum flux ($F_{\lambda,3000}$); the properties of the Mg II line (FWHM and flux); the flux of the Fe II emission and the redshift estimates $z_{\rm Mg\ II}$. We consider the 14th and 86th interquartiles of the χ^2 distribution as our 1σ confidence levels. De Rosa et al. (2014) applied a similar analysis to the spectra of ULAS 1120, VIK 0305, VIK 0109, and VIK 2348; their fitting procedures are, however, slightly different, since they fit all the spectral components at once, using the entire spectral range. Also, Venemans et al. (2015a) analyzed the NIR spectra of PSO 036+03, PSO 338+29, and PSO 167-13, considering solely the nuclear continuum emission fitted with a power law and modeling the Mg II emission line with a Gaussian function. The estimates that both studies obtain for $z_{\rm Mg\ II}$, black hole masses, and bolometric luminosities are consistent, within the uncertainties, with the ones found here (see also Section 5.6).

5.6. Black Hole Masses

We can estimate the quasar black hole masses ($M_{\rm BH}$) from our single-epoch NIR spectra using the broad Mg II emission line and $\lambda L_{\lambda,3000}$. Under the assumption that the BLR dynamics is dominated by the central black hole gravitational potential, the virial theorem states

$$M_{\rm BH} \sim \frac{R_{\rm BLR}\, v_{\rm BLR}^2}{G}, \quad (9)$$

where G is the gravitational constant and $R_{\rm BLR}$ and $v_{\rm BLR}$ are the size and the orbital velocity of the emitting clouds, respectively. The velocity can be estimated from the width of the emission line:

$$v_{\rm BLR} = f \times \text{FWHM}, \quad (10)$$

with f a geometrical factor accounting for projection effects (e.g., Decarli et al. 2008; Grier et al. 2013; Matthews et al. 2017).

Reverberation mapping techniques have been used to estimate the sizes of the BLRs from the Hβ emission lines of nearby AGNs (Peterson et al. 2004). Several studies of this kind have shown that the continuum luminosity and $R_{\rm BLR}$ of

Table 6
Parameters (Slope and Normalization) Obtained from the Power-law Fit of the Spectra in Our Quasar Sample (see Section 5.3, Equation (8))

Name	α	F_0 (10^{-17}erg s^{-1} cm^{-2})	m_{1450}	M_{1450}	$\Delta v_{\mathrm{C\,IV-Mg\,II}}$ (km s^{-1})	C IV EW (Å)
PSO J006.1240+39.2219	-3.92 ± 0.03	$0.060^{+1.86}_{-4.006}$	20.00	25.94[a]	…	…
PSO J011.3899+09.0325	$-3.75^{+3.91}_{-0.01}$	$0.051^{+0.06}_{-0.001}$	20.85	−25.95	…	…
VIK J0109–3047	$-0.96^{+2.71}_{-0.04}$	$0.141^{+0.09}_{-0.075}$	21.30	−25.58	4412 ± 175	14.9 ± 0.1
PSO J036.5078+03.0498	$-1.61^{+0.03}_{-0.07}$	0.610 ± 0.05	19.55	−27.28	5386 ± 689	41.5 ± 1.1
VIK J0305–3150	$-0.84^{+0.02}_{-0.04}$	0.203 ± 0.005	20.72	−26.13	2438 ± 137	40.5 ± 0.3
PSO J167.6415–13.4960	$-0.99^{+1.12}_{-0.68}$	$0.176^{+0.055}_{-0.175}$	21.25	−25.57	…	…
ULAS J1120+0641	$-1.35^{+0.24}_{-0.22}$	$0.248^{+0.086}_{-0.011}$	20.38	−26.58	2602 ± 285	48.1 ± 0.7
HSC J1205–0000	$-0.61^{+0.01}_{-0.48}$	$0.131^{+0.075}_{-0.275}$	21.98	−24.89	…	…
PSO J183.1124+05.0926	$-1.19^{+0.13}_{-0.15}$	$0.523^{+0.02}_{-0.05}$	19.82	−26.99	…	…
PSO J231.6576–20.8335	-1.59 ± 0.06	$0.504^{+0.003}_{-0.075}$	19.70	−27.14	5861 ± 318	23.0 ± 1.2
PSO J247.2970+24.1277	$-0.926^{+0.15}_{-0.21}$	$0.350^{+0.102}_{-0.005}$	20.28	−26.53	2391 ± 110	29.1 ± 0.7
PSO J261.0364+19.0286	$-2.01^{+1.11}_{-0.01}$	$0.166^{+0.182}_{-0.024}$	21.12	−25.69	…	…
PSO J323.1382+12.2986	$-1.38^{+0.20}_{-0.18}$	$0.227^{+0.005}_{-0.115}$	19.78	−27.06	736 ± 42	19.9 ± 0.2
PSO J338.2298+29.5089	$-1.98^{+0.87}_{-0.60}$	$0.147^{+0.035}_{-0.055}$	20.78	−26.08	842 ± 170	40.6 ± 0.8
VIK J2348–3054	$-0.65^{+1.4}_{-0.6}$	$0.155^{+0.115}_{-0.134}$	21.17	−25.74	1793 ± 110	45.8 ± 0.3

Note. We report also the apparent and absolute magnitude at rest-frame wavelength 1450 Å (Section 5.2, plotted as a function of redshift in Figure 6), the C IV blueshifts with respect to the Mg II emission lines, and the rest-frame C IV EW (Section 5.4).
[a] Value taken from Tang et al. (2017).

AGNs in the local universe correlate strongly (e.g., Kaspi et al. 2005; Bentz et al. 2013). Under the assumption that this relation holds also at high redshift, we can use $\lambda L_{\lambda,3000}$ as a proxy of the BLR size. We derive the mass of the black hole following Vestergaard & Osmer (2009):

$$\frac{M_{\mathrm{BH}}}{M_\odot} = 10^{6.86}\left(\frac{\mathrm{FWHM}}{10^3\ \mathrm{km\ s^{-1}}}\right)^2\left(\frac{\lambda L_{\lambda,3000}}{10^{44}\ \mathrm{erg\ s^{-1}}}\right)^{0.5}. \quad (11)$$

This relation has been obtained using thousands of high-quality quasar spectra from SDSS-DR3 (Schneider et al. 2005) and has been calibrated on robust reverberation mapping mass estimates (Onken et al. 2004). The scatter on its zero point of 0.55 dex, which takes into account the uncertainty in the luminosity–R_{BLR} correlation, dominates the measured uncertainties on the black hole masses.

Also, from the black hole mass we can derive the Eddington luminosity (L_{Edd}), the luminosity reached when the radiation pressure is in equilibrium with the gravitational attraction of the black hole:

$$\frac{L_{\mathrm{Edd}}}{\mathrm{erg\ s^{-1}}} = 1.3 \times 10^{38}\,\frac{M_{\mathrm{BH}}}{M_\odot}. \quad (12)$$

Another useful quantity to derive is the Eddington ratio, the total measured bolometric luminosity of the quasar (L_{bol}) divided by L_{Edd}. We estimate L_{bol} using the bolometric correction by Shen et al. (2008):

$$\frac{L_{\mathrm{bol}}}{\mathrm{erg\ s^{-1}}} = 5.15 \times \frac{\lambda L_{\lambda,3000}}{\mathrm{erg\ s^{-1}}}. \quad (13)$$

The estimated values of black hole masses, bolometric luminosities, and Eddington ratios for the quasars in our sample are shown in Table 8.

We notice that HSC 1205, the faintest object in the sample, presents a very broad Mg II emission line: this leads to a high black hole mass ($\sim 5 \times 10^9\ M_\odot$) and a low Eddington ratio of 0.06. However, HSC 1205 is also characterized by a red $J - W1$ color of 1.97, suggesting that the quasar has a red continuum, due to internal galactic extinction. This could affect our measurement of the quasar intrinsic luminosity, and therefore we could observe a value of the Eddington ratio lower than the intrinsic one. We test this hypothesis by comparing the observed photometric information of this source with a suite of quasar spectral models characterized by different values of internal reddening $E(B-V)$. We obtain these models by applying the reddening law by Calzetti et al. (2000) to a low-redshift quasar spectral template (Selsing et al. 2016), redshifted at $z = 6.73$ and corrected for the effect of the IGM absorption following Meiksin (2006). We consider the J magnitude provided by Matsuoka et al. (2016), $W1$ and $W2$ from *WISE* (see Table 3), and H and K from the VIKING survey ($H = 21.38 \pm 0.21$, $K = 20.77 \pm 0.14$). A χ^2 minimization routine suggests that this quasar has a large $E(B-V) = 0.3$. The corrected monochromatic luminosity at $\lambda_{\mathrm{rf}} = 3000$ Å is 1.62×10^{46} erg s^{-1}, and the resulting black hole mass and Eddington ratio are $7.22 \times 10^9\ M_\odot$ and 0.09, respectively. Therefore, even taking into account the high internal extinction, HSC 1205 is found to host a very massive black hole and to accrete at the lowest rate in our sample.

We now place our estimates in a wider context, comparing them with the ones derived for low-redshift quasars.

We consider the SDSS DR7 and DR12 quasar catalogs, presented by Shen et al. (2011) and Pâris et al. (2017), respectively; we select only objects in the redshift range $0.35 < z < 2.35$. In the DR7 release, we take into account the objects with any measurements of $\lambda L_{\lambda,3000}$ and Mg II FWHM (85,507 out of ∼105,000 sources). We calculate $\lambda L_{\lambda,3000}$ for the quasars in the DR12 release, modeling a continuum power law with the index provided in the catalog (entry `ALPHA_NU`) and normalizing it to the observed SDSS i magnitude. We consider only the sources in DR12 with measurements of the power-law index and of the Mg II FWHM, and not already presented in DR7. Thus, out of the 297,301 sources in DR12, we select 68,062 objects: the total number of sources is 153,569.

De Rosa et al. (2011) provide continuum luminosities and Mg II measurements for 22 quasars at $4.0 \lesssim z \lesssim 6.4$

Table 7
Quantities Derived from the Fit of the Spectral Region around the Mg II Emission Line: Monochromatic Luminosity at Rest-frame Wavelength 3000 Å (λL_{3000}); FWHM, Flux, and Redshift Estimates of the Mg II Line; and Fe II Flux

Name	λL_{3000} (10^{46} erg s^{-1})	Mg_{II} FWHM (km s^{-1})	Mg_{II} Flux (10^{-17} erg s^{-1} cm^{-2})	Fe IIFlux (10^{-17} erg s^{-1} cm^{-2})	$z_{Mg\ II}$
VIK J0109–3047	$1.0^{+0.1}_{-0.8}$	4313^{+606}_{-560}	$22.5^{+6.8}_{-6.2}$	$45^{+125}_{-0.15}$	6.763±0.01
PSO J036.5078+03.0498	$3.9^{+0.4}_{-1.2}$	4585^{+691}_{-461}	$59.4^{+11.8}_{-9.2}$	147^{+221}_{-81}	$6.533^{+0.01}_{-0.008}$
VIK J0305–3150	$1.5^{+0.2}_{-0.7}$	3210^{+450}_{-293}	$41.0^{+7.2}_{-5.0}$	42^{+124}_{-15}	$6.610^{+0.006}_{-0.005}$
PSO J167.6415–13.4960	$0.9^{+0.3}_{-0.4}$	2071^{+211}_{-354}	$8.2^{+1.4}_{-0.8}$	201	6.505 ± 0.005
ULAS J1120+0641	$3.6^{+0.4}_{-1.4}$	4258^{+524}_{-395}	$58.5^{+9.3}_{-7.8}$	61^{+225}_{-8}	$7.087^{+0.007}_{-0.009}$
HSC J1205–0000	$0.7^{+0.3}_{-0.4}$	8841^{+3410}_{-288}	$49.8^{+5.9}_{-52.4}$	<182	$6.73^{+0.01}_{-0.02}$
PSO J231.6576–20.8335	$3.7^{+0.7}_{-0.9}$	4686^{+261}_{-1800}	$87.6^{+9.0}_{-28.2}$	216^{+204}_{-128}	$6.587^{+0.012}_{-0.008}$
PSO J247.2970+24.1277	$3.4^{+0.1}_{-1.5}$	1975^{+312}_{-288}	$40.2^{+4.4}_{-5.8}$	$54^{+234}_{-0.2}$	6.476±0.004
PSO J323.1382+12.2986	$1.6^{+0.1}_{-1.0}$	3923^{+446}_{-380}	$45.9^{+7.4}_{-7.2}$	85^{+109}_{-45}	$6.592^{+0.007}_{-0.006}$
PSO J338.2298+29.5089	$0.8^{+0.4}_{-0.2}$	6491^{+543}_{1105}	$47.7^{+7.0}_{-9.0}$	76^{+44}_{-54}	$6.66^{+0.02}_{-0.01}$
VIK J2348–3054	$0.9^{+0.4}_{-0.3}$	5444^{+470}_{-1079}	$44^{+8.2}_{-8.5}$	95^{+41}_{-72}	6.902±0.01

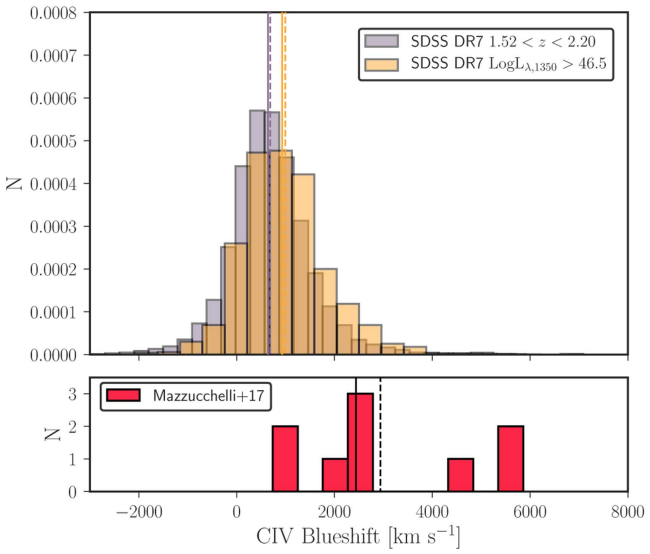

Figure 7. Histogram of C IV blueshifts with respect to the Mg II emission line, for the objects in our sample (bottom panel, red histogram) and a collection of $1.52 < z < 2.2$ quasars from the SDSS DR7 catalog (top panel, gray histogram; see text for details). A subsample of low-redshift quasars with higher luminosities ($L_{\lambda,1350} > 3 \times 10^{46}$ erg s^{-1}) is also reported (orange histogram). We adopt positive signs for blueshifts. The mean and median of the distributions are reported with solid and dashed lines, respectively. Quasars at high redshift show much higher C IV blueshifts (with values up to ∼5900 km s^{-1}) with respect to the sample at lower redshift. The histograms reported in the top panel are normalized such that the underlying area is equal to 1.

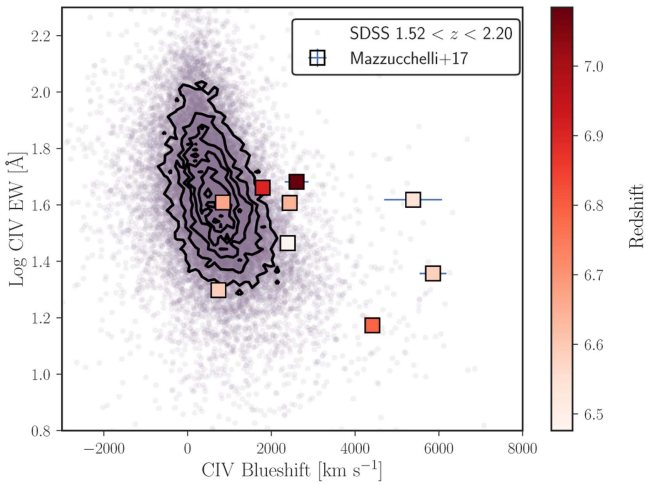

Figure 8. Rest-frame C IV EW as a function of C IV blueshift, for the quasars in our sample (big squares color-coded with respect to redshifts) and a sample of quasars at lower redshift from SDSS DR7 (Shen et al. 2011; gray circles and black contours; see text for details on the definition of this subsample). Quasars at low redshift with very high blueshifts have small EW. The high-redshift quasars are characterized by extreme blueshifts and small C IV EW, following the trend at $z \sim 1$ but with larger scatter.

(observations collected from several studies: Iwamuro et al. 2002, 2004; Barth et al. 2003; Jiang et al. 2007; Kurk et al. 2007, 2009); Willott et al. (2010a) present data for nine lower-luminosity ($L_{\rm bol} < 10^{47}$ erg s^{-1}) $z \sim 6$ quasars; finally, Wu et al. (2015) publish an ultraluminous quasar at $z \sim 6.3$. In order to implement a consistent comparison among the various data sets, we recalculate the black hole masses for all the objects in the literature using Equation (11). In Figure 10 we show $M_{\rm BH}$ versus $L_{\rm bol}$, for the quasars presented here and the objects from the aforementioned studies. We highlight regions in the parameter space with constant Eddington ratio of 0.01, 0.1, and 1; we also show the typical errors on the black hole masses, due to the method uncertainties, and on the bolometric luminosities.

We note that the quasars at $z \gtrsim 4$ are generally found at higher bolometric luminosities ($L_{\rm bol} \gtrsim 10^{46}$ erg s^{-1}) than the objects at $z \sim 1$ (also due to selection effects; see below), but that the observed black hole masses span a similar range for both samples ($10^8 \lesssim M_{\rm BH}/M_\odot \lesssim 5 \times 10^9$). The bulk of the low-redshift ($z \sim 1$) quasar population shows lower Eddington ratios than the quasars at $z \gtrsim 4$. As for the objects at $z > 6.4$ presented in this sample, they occupy a parameter space similar to the sources from De Rosa et al. (2011), with a larger scatter in bolometric luminosities.

In order to provide a consistent comparison, we study the evolution of the black hole masses and Eddington ratios, as a function of redshift, for a quasar sample matched in bolometric luminosity. Since the high-redshift quasars studied here are highly biased toward higher luminosities, mainly due to our selection criteria, a simple luminosity cut would not produce a truly luminosity-matched sample. In order to reproduce the same luminosity distribution as the one of the high-redshift sources, we sample the low-redshift SDSS quasars by randomly drawing sources with comparable $L_{\rm bol}$ to $z \gtrsim 6.5$

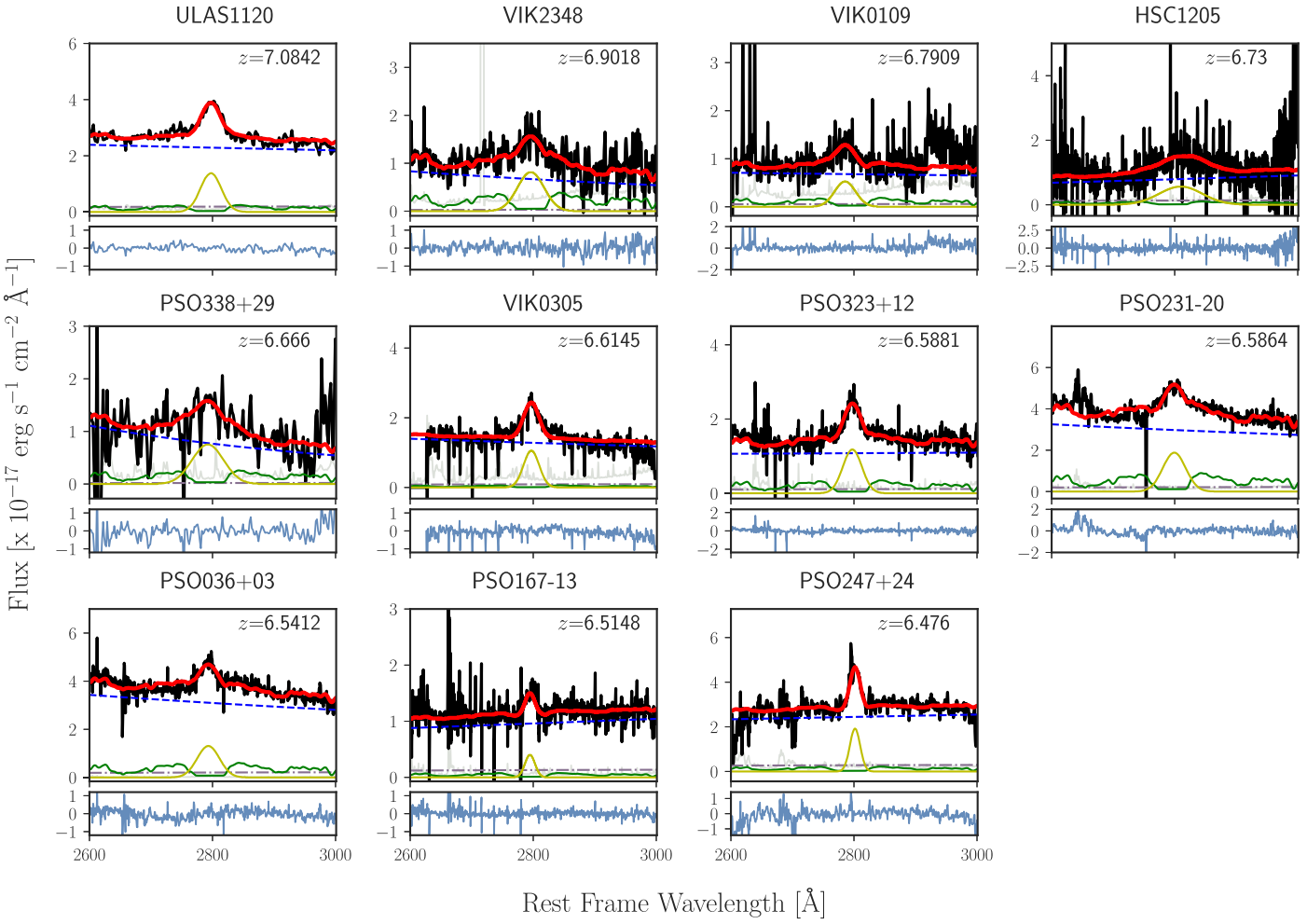

Figure 9. Best fit of the spectral region around the Mg II emission lines for the quasars in our sample for which we have *K*-band spectroscopy. We show the different components of the fit: the power-law continuum (dashed blue line), the Balmer (dot-dashed brown line) and the Fe II pseudo-continuum emission (solid green line), and the Gaussian Mg II emission line (solid yellow line); the total fit is reported with a solid red line. In the bottom panels we show the residuals of the fit. The derived quantities are listed in Table 7.

quasars (within 0.01dex); we repeat this trial 1000 times. We show in Figure 11 the black hole masses, bolometric luminosities, and Eddington ratios, as a function of redshift, for the quasars presented in this work and for objects in one of the samples drawn at $z \sim 1$. The distributions of these quantities are also reported in Figure 12. We consider, as representative values for black hole mass and Eddington ratio of a bolometric luminosity-matched sample at $z \sim 1$, the mean of the means and the mean of the standard deviations calculated from the 1000 subsamples. We then obtain $\langle \log(M_{\rm BH}) \rangle = 9.21$ and $\langle \log(L_{\rm bol}/L_{\rm Edd}) \rangle = -0.47$, with a scatter of 0.34 and 0.33, respectively. These values are consistent, also considering the large scatter, with the estimates obtained for $z \gtrsim 6.5$ quasars: $\langle \log(M_{\rm BH}) \rangle = 9.21$ and $\langle \log(L_{\rm bol}/L_{\rm Edd}) \rangle = -0.41$, with a scatter of 0.34 and 0.44, respectively. Therefore, considering a bolometric luminosity-matched sample, we do not find convincing evidence for an evolution of quasar accretion rate with redshift.

Finally, we caution that we have witnessed evidence suggesting the presence of a strong wind component in the BLR (see Sections 5.4 and 5.1). In case of non-negligible radiation pressure by ionizing photons acting on the BLRs, the black hole masses derived by the simple application of the virial theorem might be underestimated (e.g., Marconi et al. 2008). This effect depends strongly on the column density ($N_{\rm H}$) of the BLR, and on the Eddington ratio. Marconi et al. (2008) show that, in case of $0.1 \lesssim L_{\rm bol}/L_{\rm Edd} \lesssim 1.0$, as found in $z \gtrsim 6.5$ quasars, and for typical values of $10^{23} < N_{\rm H}/[{\rm cm}^{-2}] < 10^{24}$, the true black hole masses would be ∼2–10 × larger than the virial estimates. This would lead to an even stronger challenge for the current models of primordial black hole formation and growth. An in-depth discussion of this effect, given the uncertainties on the contribution of the possible wind and on the BLR structure itself, is beyond the scope of this paper.

5.7. Black Hole Seeds

Measurements of black hole masses and Eddington ratios of high-redshift quasars help us constrain formation scenarios of the first supermassive black holes in the very early universe. While the black hole seeds from Population III stars are expected to be relatively small (∼100 $M_{\odot}$; e.g., Valiante et al. 2016), direct collapse of massive clouds can lead to the formation of more massive seeds ($\sim 10^4 - 10^6$ $M_{\odot}$; for a review see Volonteri 2010). In general, the time in which a black hole of mass $M_{\rm BH,f}$ is grown from an initial seed $M_{\rm BH,seed}$, assuming that it accretes with a constant Eddington ratio for all the time, can be written as

Table 8
Estimated Quantities for the Quasars in Our Sample: Bolometric Luminosities, Black Hole Masses, Eddington Ratios, Fe II/Mg II Flux Ratios

Name	$L_{\rm bol}$ (10^{47} erg s^{-1})	M_{BH} ($\times 10^9\,M_\odot$)	$L_{\rm bol}/L_{\rm edd}$	Fe II/Mg II
VIK J0109–3047	$0.51^{+0.05}_{-0.06}$	$1.33^{+0.38}_{-0.62}$	$0.29^{+0.88}_{-2.59}$	$2.02^{+5.56}_{-0.65}$
PSO J036.5078+03.0498	$2.0^{+0.22}_{-0.64}$	$3.00^{+0.92}_{-0.77}$	$0.51^{+0.17}_{-0.21}$	$2.47^{+3.71}_{-1.36}$
VIK J0305–3150	$0.75^{+0.10}_{-0.34}$	$0.90^{+0.29}_{-0.27}$	$0.64^{+2.20}_{-3.42}$	$1.03^{+3.04}_{-0.37}$
PSO J167.6415–13.4960	$0.47^{+0.16}_{-0.22}$	$0.30^{+0.08}_{-0.12}$	$1.22^{+0.51}_{-0.75}$	<3.1
ULAS J1120+0641	$1.83^{+0.19}_{-0.072}$	$2.47^{+0.62}_{-0.67}$	$0.57^{0.16}_{0.27}$	$1.04^{+3.84}_{-0.14}$
HSC J1205–0000	$0.36^{+0.18}_{-0.20}$	$4.7^{+1.2}_{-3.9}$	$0.06^{+0.32}_{-0.58}$	<0.50
PSO J231.6576–20.8335	$1.89^{+0.34}_{-0.45}$	$3.05^{+0.44}_{-2.24}$	$0.48^{+0.11}_{-0.39}$	2.64 ± 1.7
PSO J247.2970+24.1277	$1.77^{+0.06}_{-0.76}$	$0.52^{+0.22}_{-0.25}$	$2.60^{+0.08}_{-0.15}$	$1.33^{+5.82}_{-0.01}$
PSO J323.1382+12.2986	$0.81^{+0.07}_{-0.50}$	$1.39^{+0.32}_{-0.51}$	$0.44^{+1.09}_{-3.19}$	$1.85^{+2.37}_{-0.97}$
PSO J338.2298+29.5089	$4.04^{+2.14}_{-0.90}$	$2.70^{+0.85}_{-0.97}$	$0.11^{+0.71}_{-0.49}$	$1.29^{+2.1}_{-0.74}$
VIK J2348–3054	$0.43^{+0.20}_{-0.13}$	$1.98^{+0.57}_{-0.84}$	$0.17^{+0.92}_{-0.88}$	$2.13^{+0.93}_{-1.54}$

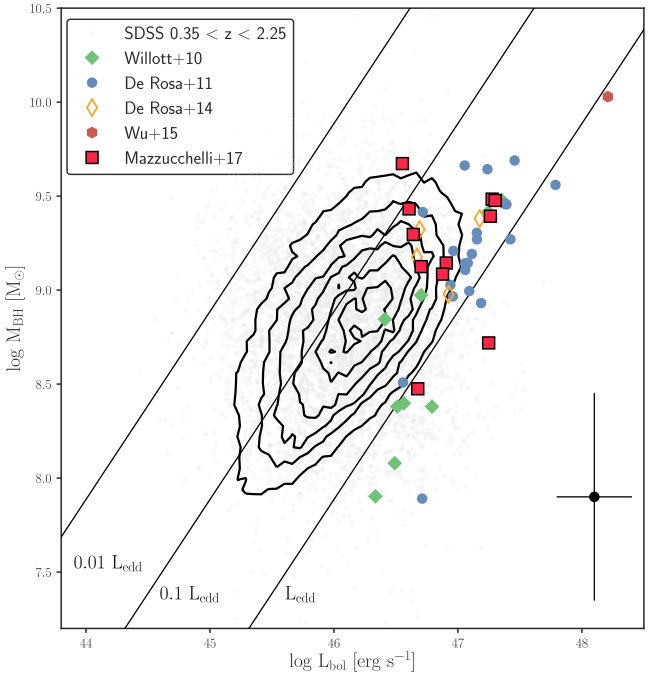

Figure 10. Black hole mass as a function of bolometric luminosity for several quasar samples. We report a subsample from the SDSS DR7 and DR12 quasar catalogs (Shen et al. 2011 and Pâris et al. 2017, respectively) at $0.35 < z < 2.25$ (gray circles and contours). Also, we show measurements for quasars at higher redshifts, from Willott et al. (2010a, $z \sim 6$; green filled diamonds), De Rosa et al. (2011, $4 < z < 6.4$; blue circles), and Wu et al. (2015, $z \sim 6.3$; dark red hexagon). The objects presented in this study are reported with red filled squares. We notice that four quasars (VIK0109, VIK 0305, VIK 2348, and ULAS 1120) have also been analyzed by De Rosa et al. (2014, orange open diamonds); the two sets of measurements are consistent within the error bars. We show the method uncertainties on the black hole mass estimates and a representative mean error on the bolometric luminosity measurements (black point), and regions in the parameter space with constant Eddington luminosity (black lines). Quasars at high redshift are generally characterized by higher Eddington ratios than their lower-redshift counterparts, suggesting that they accrete at higher rates. However, the scatter in the $z \gtrsim 6.5$ sample is not negligible, with objects at $L_{\rm bol}/L_{\rm Edd}$ as low as ~0.1.

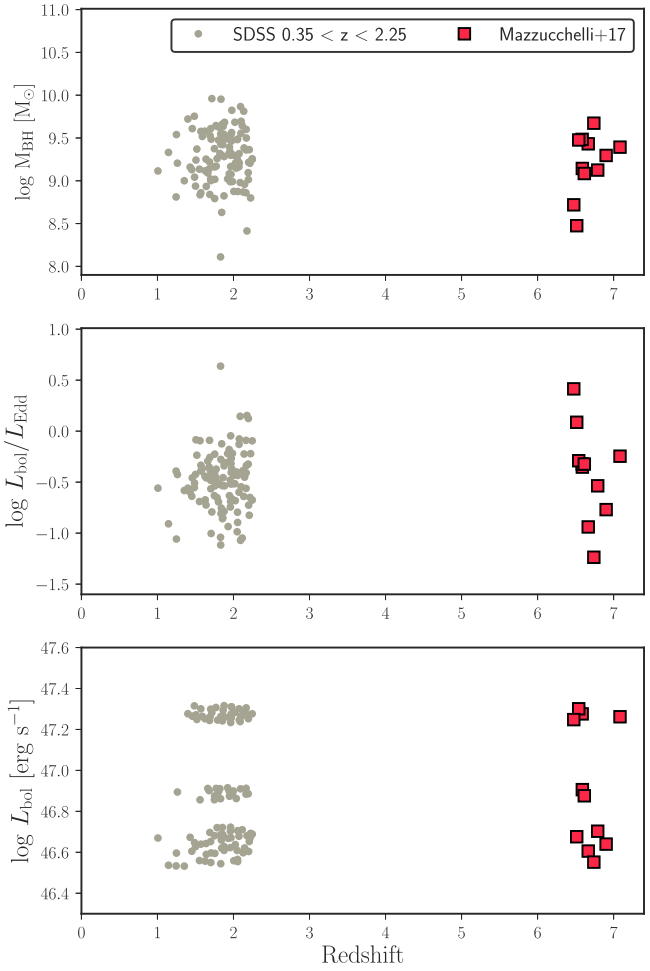

Figure 11. Black hole mass (top panel), Eddington ratio (middle panel), and bolometric luminosity (bottom panel) against redshift, for a bolometric luminosity-matched quasar sample (see text for details on the selection of the subsample at $z \sim 1$). We report the $z \gtrsim 6.5$ quasars presented in this work with red squares and the ones at lower redshift ($0.35 < z < 2.25$) from SDSS DR7 +DR12 (Shen et al. 2011; Pâris et al. 2017) with gray circles. The mean values of quasar black hole masses and Eddington ratios do not vary significantly with redshift (see also Figure 12).

(Shapiro 2005; Volonteri & Rees 2005)

$$\frac{t}{\rm Gyr} = t_{\rm s} \times \left[\frac{\epsilon}{1-\epsilon}\right] \times \frac{L_{\rm Edd}}{L_{\rm bol}} \times \ln\left(\frac{M_{\rm BH,f}}{M_{\rm BH,seed}}\right), \qquad (14)$$

where $t_{\rm s} = 0.45$ Gyr is the Salpeter time and $\epsilon \sim 0.07$ is the radiative efficiency (Pacucci et al. 2015). The average $M_{\rm BH}$ and $L_{\rm bol}/L_{\rm Edd}$ of all the $z \gtrsim 6.5$ quasars in the sample presented

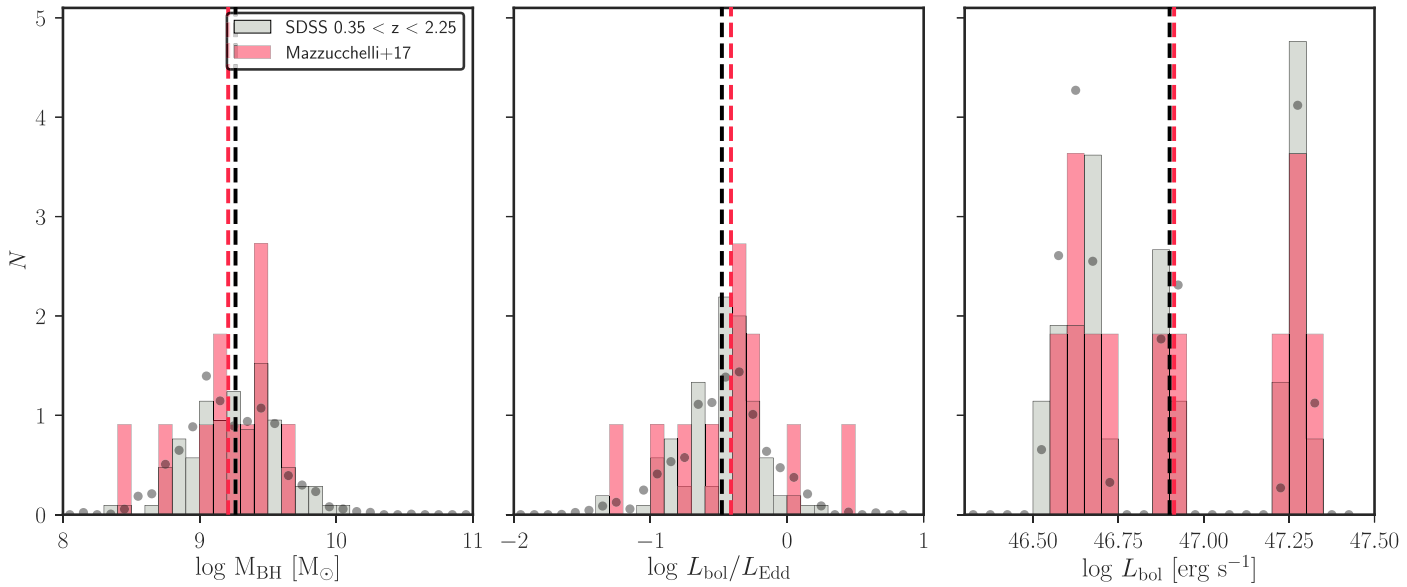

Figure 12. Distribution of black hole masses (left panel), Eddington ratios (middle panel), and bolometric luminosities (right panel) for one of the 1000 bolometric luminosity-matched subsamples drawn from low-redshift SDSS quasars (gray histograms; Shen et al. 2011 and Pâris et al. 2017; see text for details), and for the $z \gtrsim 6.5$ quasars presented here (red histograms). The gray circles represent the mean of black hole masses, Eddington ratios, and bolometric luminosities in each bin, resulting from all the 1000 trials at $z \sim 1$. The mean of each quantity, for the low- and high-redshift populations, is shown in each panel with black and red dashed lines, respectively. We note that the mean black hole masses and Eddington ratios of the two samples are consistent, suggesting a non-evolution of accretion rate with cosmic time. The histograms are normalized such that the underlying area is equal to 1.

here (11 objects, not considering any luminosity cut; see Table 8) are $1.62 \times 10^9\ M_\odot$ and 0.39, respectively. If we insert these values in Equation (14), we can calculate the time needed by a black hole seed of $M_{\rm BH,seed} = [10^2, 10^4, 10^5, 10^6]\ M_\odot$ to grow to the mean $M_{\rm BH}$ found here, assuming that it always accretes at an average Eddington rate of ∼0.39. We find that this time is $t = [1.44, 1.04, 0.84, 0.64]$ Gyr. As the age of the universe at $z \sim 6.5$ is only ∼0.83 Gyr, this implies that only very massive seeds ($\sim 10^6\ M_\odot$) would be able to form the observed supermassive black holes.

Alternatively, we can invert Equation (14) and derive the initial masses of the black hole seeds required to obtain the observed black holes. This result depends on the assumptions made, e.g., on the redshift of the seed formation (z_i), on the accretion rate ($L_{\rm bol}/L_{\rm Edd}$), and on the radiative efficiency (ϵ; see Equation (14)).[24] We here consider different values for these parameters: we assume that the black holes accrete constantly with the observed Eddington ratios or with $L_{\rm bol}/L_{\rm Edd} = 1$; also, we consider that they grow for a period of time equal to the age of the universe at their redshifts (i.e., $z_i \Rightarrow \infty$), and from $z_i = 30$ or 20 (see different rows in Figure 13). Finally, we assume an efficiency of 7% or 10% (left and right columns in Figure 13). The derived values of black hole seeds for all the combinations of these parameters are shown in Figure 13. In all the cases considered here with $\epsilon = 0.07$ and Eddington accretion (and in case of $\epsilon = 0.1$, $z_i \Rightarrow \infty$ and $L_{\rm bol}/L_{\rm Edd} = 1$), the calculated seed masses ($\gtrsim 10^2\ M_\odot$) are consistent with being formed by stellar remnants. Alternatively, a scenario of higher efficiency ($\epsilon = 0.1$), later seed birth (i.e., $z = 30$ or 20), and accretion at $L_{\rm bol}/L_{\rm Edd} = 1$ would require more massive seeds ($\sim 10^{3\text{-}4}\ M_\odot$) as progenitors of the observed $z \gtrsim 6.5$ quasars.

[24] The efficiency depends in turn on the black hole spin and can be as high as ∼40% in the case of maximally spinning black holes. The spin is still an elusive parameter; it has been observationally measured only in ∼20 sources in the local universe (through the relativistic broadening of the Fe Kα line; Brenneman et al. 2011; Reynolds 2014). Thanks to stacked *Chandra* deep observations of ∼30 lensed quasars, Walton et al. (2015) detected a broadened component of the Kα line up to $z \sim 4.5$; however, the low S/N prevented a measurement of the single quasars' black hole spins. Current semianalytical models place only weak constraints on the spin value at $z \gtrsim 5$, which depends on the gas accretion mode, galactic morphology, and black hole mass (e.g., Sesana et al. 2014). However, since the spin decreases with black hole mass, we do not expect large values for our sample of quasars with $M_{\rm BH} \gtrsim 10^8\ M_\odot$.

5.8. Fe II/ Mg II

The estimate of the relative abundances of metals in high-redshift sources is a useful proxy in the investigation of the chemical composition and evolution of galaxies in the early universe. In this context, the Mg II/Fe II ratio is of particular interest: α-elements, such as Mg, are mainly produced via Type II supernovae (SNe) involving massive stars, while Type Ia SNe from binary systems are primarily responsible for the provision of iron (Nomoto et al. 1997). Given that SNe Ia are expected to be delayed by ∼1 Gyr (Matteucci & Greggio 1986) with respect to SNe II, estimating the relative abundances of α-elements to iron provides important insights on the stellar population in the galaxy and on the duration and intensity of the star formation burst. Tracking the evolution of the Mg II/ Fe II ratio as a function of redshift allows us to reconstruct the evolution of the galactic star formation history over cosmic time.

Many studies in the literature investigate the Mg II/Fe II ratio in the BLR of quasars, by estimating the ratio of the Fe II and Mg II fluxes ($F_{\rm Fe\,II}/F_{\rm Mg\,II}$), considered a first-order proxy of the abundance ratio (e.g., Iwamuro et al. 2002, 2004; Barth et al. 2003; Maiolino et al. 2003; Jiang et al. 2007; Kurk et al. 2007; Sameshima et al. 2009; De Rosa et al. 2011, 2014). In particular, De Rosa et al. (2011, 2014) present a consistent analysis of ∼30 quasar spectra in the redshift range $4 \lesssim z \lesssim 7.1$ and find no evolution of their $F_{\rm Fe\,II}/F_{\rm Mg\,II}$ with cosmic time. We estimate the Fe II and Mg II fluxes for the quasars in our study following De Rosa et al. (2014): for the

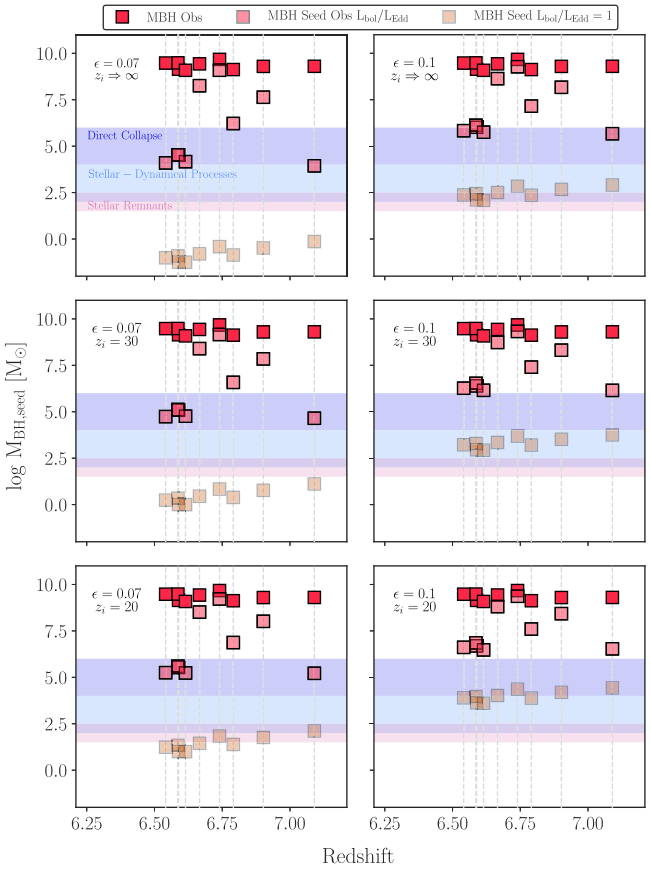

Figure 13. Masses of the black hole seeds required to obtain the observed black hole masses in our quasar sample (dark red squares). We here vary the efficiency ($\epsilon = 0.07/0.1$, left and right columns) and the redshift of the seed formation ($z \Rightarrow \infty/30/20$, from top to bottom). For each case, we assume that the sources accrete constantly with the observed Eddington ratio (light-red squares; see also Table 8) and at Eddington rate (yellow squares). The ranges of black hole seeds predicted by current theoretical models are shown in orange, light-blue, and dark-blue shaded areas (see text for references). Black hole seeds with masses $\gtrsim 10^2$ $M_\odot$ can produce the observed high-redshift quasars in all cases with $\epsilon = 0.07$ and $L_{bol}/L_{Edd} = 1$, and in case of [$\epsilon = 0.1$, $L_{bol}/L_{Edd} = 1$ and $z_i \Rightarrow \infty$]. If the efficiency is higher (10%) and the seeds form at $z \sim 30$–20, their predicted masses are correspondingly larger ($\sim 10^{3-4}$ $M_\odot$, at Eddington accretion).

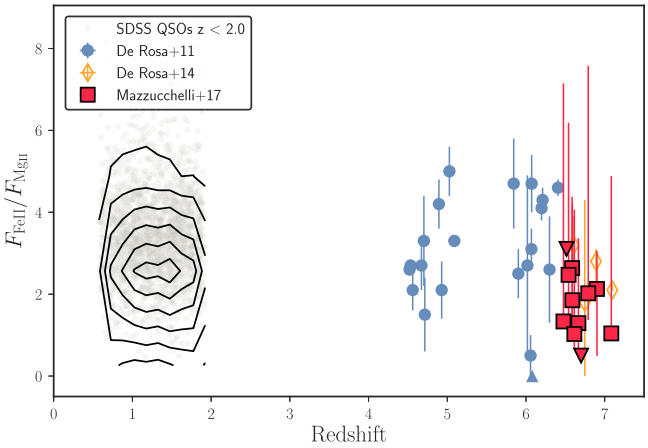

Figure 14. Fe II/Mg II flux ratio, considered as a first-order proxy for the relative abundance ratio, vs. redshift. We show the quasars in our sample (red squares and, in case of upper limits, downward-pointing triangles) and taken from the literature: De Rosa et al. (2011; blue circles) and $z \lesssim 2$ SDSS quasars (Calderone et al. 2017, gray circles and black contours). We show with orange open diamonds the measurements of De Rosa et al. (2014) for four of our quasars (VIK 0109, VIK 0305, VIK 2348, and ULAS 1120); they have been derived with a slightly different fitting routine (see text for details) but are consistent, within the errors, with the estimates obtained here. Our measurements are systematically lower than those of samples at lower redshifts; however, taking into account the large uncertainties, we find no statistical evidence for an evolution of the flux ratio with redshift.

former we integrate the fitted iron template over the rest-frame wavelength range $2200 < \lambda$ [Å] < 3090, and for the latter we compute the integral of the fitted Gaussian function (see Tables 7 and 8 for the estimated flux values). In Figure 14, we plot $F_{Fe\,II}/F_{Mg\,II}$ as a function of redshift, for both the quasars in our sample and sources from the literature. We consider the sample by De Rosa et al. (2011, 2014) and a sample of low-redshift quasars ($z \lesssim 2.05$) from Calderone et al. (2017). They consistently re-analyzed a subsample of quasars (~70,000) from the SDSS-DR10 catalog and provide measurements of the flux for Mg, Fe, and the continuum emission at rest-frame $\lambda_{rf} = 3000$ Å.[25] Here, we take only the sources with no flag on the quantities above (~44,000 objects), and we correct the Fe II flux to account for the different wavelength ranges where the iron emission was computed.[26] From Figure 14, we see that the flux ratios of the quasars in our sample are systematically lower than the ones of the sources at lower redshift, both from De Rosa et al. (2011) and from Calderone et al. (2017): this suggests a possible depletion of iron at $z \gtrsim 6.5$, and therefore the presence of a younger stellar population in these quasar host galaxies. However, our estimates are also characterized by large uncertainties, mainly due to the large uncertainties on the iron flux estimates (see Table 7). Within the errors, our measurements are consistent with a scenario of non-evolving $F_{Fe\,II}/F_{Mg\,II}$ over cosmic time, in agreement with De Rosa et al. (2014). We test whether the systematic lower values of $F_{Fe\,II}/F_{Mg\,II}$ for the highest-redshift quasar population are statistically significant. We associate with each of our measurements a probability distribution, built by connecting two half-Gaussian functions with mean and σ equal to the calculated ratio and to the lower (or upper) uncertainty, respectively. We sum these functions to obtain the total probability distribution for the objects at high redshift. We compare this function with the distribution of the $F_{Fe\,II}/F_{Mg\,II}$ values for the quasars at $z \sim 1$. We randomly draw nine sources from the two distributions (the objects in our sample excluding the limits), and we apply a Kolmogorov-Smirnov test to check whether these two samples could have been taken from the same probability distribution; we repeat this draw 10,000 times. We obtain that the p-value is greater than 0.2 (0.5) in 51% (27%) of the cases; this highlights that, considering the large uncertainties, we do not significantly measure a difference in the total probability distribution of $F_{Fe\,II}/F_{Mg\,II}$ at low and high redshift. Data with higher S/N in the Fe II emission line region are needed to place more stringent constraints on the evolution of the abundance ratio.

5.9. Infrared and [C II] Luminosities

We observed four quasars in our sample with NOEMA (see Section 3). We extract their spectra and fit the continuum

[25] http://qsfit.inaf.it/

[26] Calderone et al. (2017) integrate the iron template in the rest-frame wavelength range $2140 < \lambda$[Å] < 3090, while we use the range $2200 < \lambda$[Å] < 3090.

Table 9
Results from Our NOEMA Observations:

	HSC J1205–0000	PSO J338.2298+29.5089	PSO J006.1240+39.2219	PSO J323.1283+12.2986
$z_{[\mathrm{C\,II}]} - z_{\mathrm{MgII}}$ [km s^{-1}]	···	818^{+168}_{-138}	···	230 ± 13
[C ii] line width [km s^{-1}]	···	740^{+541}_{-313}	277^{+161}_{-141}	254^{+48}_{-28}
[C ii] flux [Jy km s^{-1}]	···	$1.72^{+0.91}_{-0.84}$	$0.78^{+0.54}_{-0.38}$	$1.05^{+0.33}_{-0.21}$
Continuum flux density [mJy]	0.833 ± 0.176	0.972 ± 0.215	0.548 ± 0.178	0.470 ± 0.146
$L_{[\mathrm{C\,II}]}$ [$10^9\,L_\odot$]	···	2.0 ± 0.1	$0.9^{+0.6}_{-0.4}$	$1.2^{+0.4}_{-0.2}$
L_{FIR} [$10^{12}\,L_\odot$]	1.9 ± 0.4	2.1 ± 0.5	1.1 ± 0.4	1.0 ± 0.3
L_{TIR} [$10^{12}\,L_\odot$]	2.6 ± 0.5	2.8 ± 0.6	1.5 ± 0.5	1.3 ± 0.4
$L_{[\mathrm{C\,II}]}/L_{\mathrm{FIR}}$ [10^{-3}]	···	$0.98^{+0.55}_{-0.52}$	$0.77^{+0.59}_{-0.45}$	$1.2^{+0.54}_{-0.45}$

Note. We report the [C II] line and continuum emission quantities obtained from our fit (i.e., flux and line width) and the [C II] line, FIR, and TIR luminosities.

+[C II] line emission with a flat+Gaussian function (see Figure 4). We estimate the line properties, e.g., the peak frequency, the width, amplitude, and flux, and we calculate the continuum flux at rest-frame wavelength 158 μm from the continuum map. We report these values in Table 9.

We can derive the far-infrared (FIR) properties of the observed quasars, following a number of assumptions commonly presented in the literature (e.g., Venemans et al. 2012, Venemans et al. 2016). We approximate the shape of the quasar infrared emission with a modified blackbody: $f_\nu \propto B_\nu(T_d)(1 - e^{\tau_d})$, where $B_\nu(T_d)$ is the Planck function and T_d and τ_d are the dust temperature and optical depth, respectively (Beelen et al. 2006). Under the assumption that the dust is optically thin at wavelength $\lambda_{\mathrm{rf}} > 40\ \mu$m ($\tau_d \ll 1$), we can further simplify the function above as $f_\nu \propto B_\nu(T_d)\nu^\beta$, with β the dust emissivity power-law spectral index. We take $T_d = 47$ K and $\beta = 1.6$, which are typical values assumed in the literature (Beelen et al. 2006). We scale the modified blackbody function to the observed continuum flux at the rest-frame frequency $\nu_{\mathrm{rf}} = 1900$ GHz; we then calculate the FIR luminosity (L_{FIR}) integrating the template in the rest-frame wavelength range 42.5−122.5 μm (Helou et al. 1988). The total infrared (TIR) luminosity (L_{TIR}) is defined instead as the integral of the same function from 8 to 1000 μm. We note that these luminosity values are crucially dependent on the assumed shape of the quasar infrared emission, which, given the poor photometric constraints available, is highly uncertain. We can also calculate the luminosity of the [C II] emission line ($L_{[\mathrm{C\,II}]}$) from the observed line flux ($S_{[\mathrm{C\,II}]}\Delta v$; Carilli & Walter 2013):

$$\frac{L_{[\mathrm{C\,II}]}}{L_\odot} = 1.04 \times 10^{-3} \frac{S_{[\mathrm{C\,II}]}\Delta v}{\mathrm{Jy\ km\ s^{-1}}} \left(\frac{D_{\mathrm{L}}}{\mathrm{Mpc}}\right)^2 \frac{\nu_{\mathrm{obs}}}{\mathrm{GHz}}, \quad (15)$$

where D_{L} is the luminosity distance and ν_{obs} is the observed frequency. In Table 9, we list our estimates for the [C II], FIR, and TIR luminosities.

In Figure 15, we plot $L_{[\mathrm{C\,II}]}/L_{\mathrm{FIR}}$ versus L_{FIR} for the quasars studied here and for a variety of sources from the literature. At low redshift ($z < 1$) both star-forming galaxies (Malhotra et al. 2001; Sargsyan et al. 2014) and more extreme objects, e.g., LIRGs and ULIRGs (Diaz-Santos et al. 2013; Farrah et al. 2013), show lower luminosity ratios at higher FIR luminosities; this phenomenon is known as the "C II-deficit." At $z > 1$, the scenario is less clear, where the scatter in the measurements of $L_{[\mathrm{C\,II}]}/L_{\mathrm{FIR}}$ for star-forming galaxies (Stacey et al. 2010; Brisbin et al. 2015; Gullberg et al. 2015), submillimeter galaxies (SMGs), and quasars increases. Quasars at $z > 5$ present a variety of $L_{[\mathrm{C\,II}]}/L_{\mathrm{FIR}}$ values, mostly depending on their FIR brightness. Walter et al. (2009) and Wang et al. (2013) observe quasars with high L_{FIR} and show that they are characterized by low luminosity ratios, comparable to local ULIRGs ($\langle \log(L_{[\mathrm{C\,II}]}/L_{\mathrm{FIR}})\rangle \sim -3.5$). On the other hand, quasars with lower FIR luminosities and black hole masses ($M_{\mathrm{BH}} < 10^9\ M_\odot$; Willott et al. 2015) are located in a region of the parameter space similar to the one of regular star-forming galaxies ($\langle \log(L_{[\mathrm{C\,II}]}/L_{\mathrm{FIR}})\rangle \sim -2.5$). In the literature, the decrease of $L_{[\mathrm{C\,II}]}$ in high-redshift quasars has been tentatively explained invoking a role of the central AGN emission, which is heating the dust. The problem is, however, still under debate, and several other alternative scenarios have been advocated, e.g., C^+ suppression due to X-ray radiation from the AGN (Langer & Pineda 2015), or the relative importance of different modes of star formation ongoing in the galaxies (Gracia-Carpio et al. 2011). The quasars whose new infrared observations are presented here, with $L_{\mathrm{FIR}} \sim 10^{12}\,L_\odot$, are characterized by values of the luminosity ratio in between the ones of FIR-bright quasars and of the sample by Willott et al. (2014; $\langle \log(L_{[\mathrm{C\,II}]}/L_{\mathrm{FIR}})\rangle \sim -3.0$). This is similar to what was found by Venemans et al. (2012, 2017) for ULAS 1120 and suggests that the host galaxies of these quasars are more similar to ULIRGs.

5.10. Near Zones

Near zones are regions surrounding quasars where the IGM is ionized by the UV radiation emitted from the central source. Taking into account several approximations, e.g., that the IGM is partially ionized and solely composed of hydrogen, and that photoionization recombination equilibrium is found outside the ionized region (Fan et al. 2006), the radius of the ionized bubble can be expressed as

$$R_s \propto \left(\frac{\dot{N}_Q t_Q}{f_{\mathrm{H\,I}}}\right)^{1/3}, \quad (16)$$

where $\dot{N}_Q$ is the rate of ionizing photons produced by the quasar, t_Q is the quasar lifetime, and $f_{\mathrm{H\,I}}$ is the IGM neutral fraction. Several studies provide estimates of near-zone radii for samples of $z > 5$ quasars and investigate its evolution as a function of redshift, in order to investigate the IGM evolution (Fan et al. 2006; Carilli et al. 2010; Venemans et al. 2015a; Eilers et al. 2017).

However, it is not straightforward to derive the exact values of R_s from the observed spectra; instead, we calculate here the near-zone radii (R_{NZ}) for the sources in our sample. We follow the definition of Fan et al. (2006), i.e., R_{NZ} is the distance from the central source where the transmitted flux drops below 0.1, once the spectrum has been smoothed to a resolution of 20 Å.

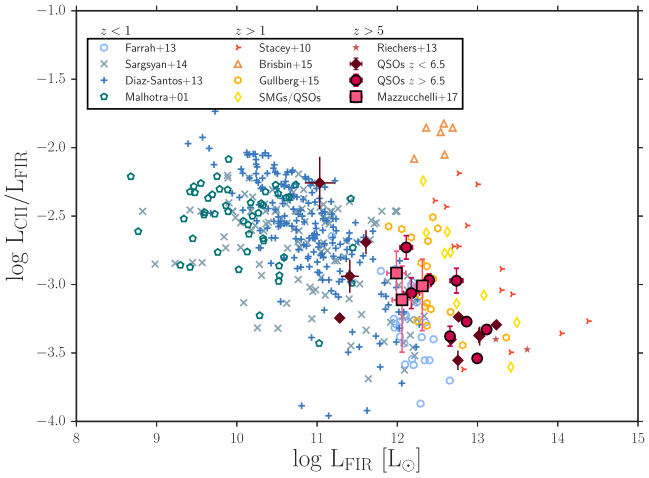

Figure 15. [C II]-to-FIR luminosity ratio as a function of FIR luminosity. With open blue/green symbols we report objects at $z < 1$: star-forming galaxies (Malhotra et al. 2001, Sargsyan et al. 2014), LIRGs (Diaz-Santos et al. 2013), and ULIRGs (Farrah et al. 2013). Values for sources at $1 < z < 5$ are shown with open yellow/orange symbols: star-forming galaxies (Stacey et al. 2010, Brisbin et al. 2015; Gullberg et al. 2015) and a collection of $3 \lesssim z \lesssim 5$ submillimeter galaxies and quasars (Maiolino et al. 2009; Wagg et al. 2010, 2012; Ivison et al. 2010; Cox et al. 2011; De Breuck et al. 2011; Valtchanov et al. 2011; Walter et al. 2012). The $z = 6.3$ SMG presented in Riechers et al. (2013) is shown as a light-red star. Quasars at $5 \lesssim z \lesssim 6.5$ (Maiolino et al. 2005, Wang et al. 2013; Willott et al. 2015) are shown with filled dark-pink diamonds. Quasars in the sample presented here are reported with filled light-pink squares (new observations for PSO 338+29, PSO 323+12, PSO 006+39) and with filled pink circles (data taken from the literature; ULAS J1120, Venemans et al. 2012; PSO 036+03, Bañados et al. 2015b; VIK J0109, VIK J0305, VIK J2348, Venemans et al. 2016; PSO 231-20, PSO 183+05, PSO 167-13, R. Decarli et al., in preparation). Local sources show a decrease in the [C II]-to-FIR ratio at high FIR luminosities, whereas the values of this ratio for the high-redshift sample have a large scatter. The $z > 6$ quasars whose millimeter observations are presented in this work are characterized by values of $L_{[\mathrm{C\,II}]}/L_{\mathrm{FIR}}$ comparable to local ULIRGs. The range of [C II]-to-FIR luminosity ratio of the general population of $z > 6$ quasars, however, hints to an intrinsic diversity among their host galaxies.

The transmitted flux is obtained by dividing the observed spectrum by a model of the intrinsic emission. We here model the quasar emission at $\lambda_{\mathrm{rf}} < 1215.16$ Å using a principal component analysis (PCA) approach: the total spectrum, $q(\lambda)$, is represented as the sum of a mean spectrum, $\mu(\lambda)$, and $n = 1,..,N$ principal component spectra (PCS), $\xi_n(\lambda)$, each weighted by a coefficient w_n:

$$q(\lambda) = \mu(\lambda) + \sum_{n=1}^{N} w_n \xi_n(\lambda). \quad (17)$$

Pâris et al. (2011) and Suzuki (2006) apply the PCA to a collection of 78 $z \sim 3$ and 50 $z \lesssim 1$ quasars from SDSS, respectively. In our study, we follow the approach by Eilers et al. (2017), mainly referring to Pâris et al. (2011), who provide PCS functions within the rest-frame wavelength window $1020 < \lambda[\text{Å}] < 2000$. After normalizing our spectra to the flux at $\lambda_{\mathrm{rf}} = 1280$ Å, we fit the region redward of the Lyα emission line ($\lambda_{\mathrm{rf}} > 1215.16$ Å) to the PCS by Pâris et al. (2011), and we derive the best coefficients by finding the maximum likelihood. We then obtain the best coefficients that reproduce the entire spectrum by using the projection matrix presented by Pâris et al. (2011). For further details on this modeling procedure, see Eilers et al. (2017). We show in Figure 16 an example of PCA for one of the quasars in our sample. Also, in this way we provide an analysis of the near-zone sizes consistent with Eilers et al. (2017), making it possible to coherently compare the results obtained from the two data sets.

The near-zone sizes depend also on quasar luminosity (through the $\dot{N}_Q$ term in Equation (16)): if we want to study their evolution with redshift, we need to break this degeneracy. We re-scale the quasar luminosities to the common value of $M_{1450} = -27$ (following previous studies; e.g., Carilli et al. 2010; Venemans et al. 2015a), and we use the scaling relation obtained from the most recent numerical simulations presented in Eilers et al. (2017) and F. Davies et al. (in preparation). They simulate radiative transfer outputs for a suite of $z = 6$ quasars within the luminosity range $-24.78 < M_{1450} < -29.14$ and constantly shining over $10^{7.5}$ yr, considering two scenarios in which the surrounding IGM is mostly ionized (as supported at $z \sim 6$ by recent studies; e.g., McGreer et al. 2015) or mostly neutral. They obtain comparable results for the two cases, which are both in agreement with the outcome obtained by fitting the observational data (see Eilers et al. 2017, Figure 5). Following the approach of Eilers et al. (2017), we consider the case of a mostly ionized IGM: they fit the simulated quasar near-zone sizes against luminosity with the power law

$$R_{\mathrm{NZ}} = 5.57\ \mathrm{pMpc} \times 10^{0.4(M_{1450})/2.35}, \quad (18)$$

with pMpc being proper Mpc, from which they derive the following scaling relation, which we also use here:

$$R_{\mathrm{NZ,corr}} = R_{\mathrm{NZ}}\ 10^{0.4(27+M_{1450})/2.35}. \quad (19)$$

We report in Table 10 the derived quantities, and the transmission fluxes are shown in Figure 17. We do not consider in our analysis the following quasars: HSC 1205, due to the poor quality of the spectrum in the Lyα emission region (see Figure 3); PSO 183+05, since this quasar is believed to present a proximate ($z \approx 6.404$) DLA (see Chen et al. 2016; E. Bañados et al., in preparation); and PSO 011+09 and PSO 261+19. These last two objects were discovered very recently, and the only redshift measurements are provided by the Lyα emission line; the lack of any other strong emission line, and the broad shape of the Lyα line, do not permit us to rule out that these quasars are BAL objects. The redshifts of the remaining objects are mainly derived from [C II] observations (see Table 10).

We show the evolution of $R_{\mathrm{NZ,corr}}$ as a function of redshift in Figure 18. We compare our data with estimates at lower redshift ($5.6 \lesssim z \lesssim 6.6$) presented by Eilers et al. (2017). The best fit of the evolution of $R_{\mathrm{NZ,corr}}$ with z, modeled as a power-law function, gives the following:

$$R_{\mathrm{NZ,corr}} = (4.49 \pm 0.92) \times \left(\frac{1+z}{7}\right)^{-1.00\pm0.20}. \quad (20)$$

The values obtained are consistent, within the errors, with the results of Eilers et al. (2017).[27] In agreement with both measurements from observations and radiative transfer simulations presented by Eilers et al. (2017), we find a weak evolution of the quasar near-zone sizes with cosmic time: this evolution is indeed much shallower than what was obtained by previous works (Fan et al. 2006; Carilli et al. 2010; Venemans et al.

[27] $R_{\mathrm{NZ,corr}} \approx 4.87 \times [(1+z)/7]^{-1.44}$; see also their Figure 6.

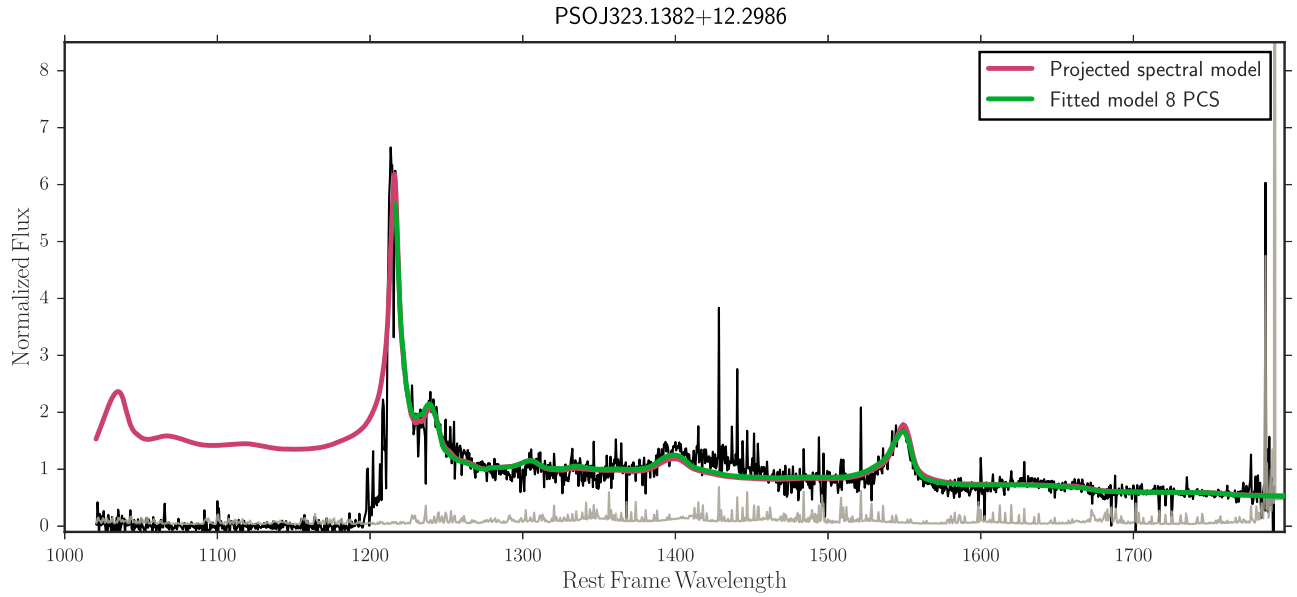

Figure 16. Example of quasar continuum emission fit with the PCA method for one of the sources in our sample (PSO 323+12). We show the fitted model at wavelengths greater than the Lyα emission line (with eight PCAs; green line) and the projected model on the entire spectrum (purple line).

Table 10
Near-zone Sizes of 11 Quasars in the Sample Presented Here

Name	$R_{\rm NZ}$ (Mpc)	$R_{\rm NZ,corr}$ (Mpc)	$R_{\rm NZ,corr,err}$ (Mpc)	PCS
PSO J006.1240+39.2219	4.47	6.78	0.09	5
VIK J0109–3047	1.59	2.78	0.03	8
PSO J036.5078+03.0498	4.37	3.91	0.08	8
VIK J0305–3150	3.417	4.81	0.006	10
PSO J167.6415–13.4960	2.02	3.55	0.03	8
ULAS J1120+0641	2.10	2.48	0.02	9
PSO J231.6576–20.8335	4.28	4.05	0.03	8
PSO J247.2970+24.1277	2.46	2.96	0.24	5
PSO J323.1382+12.2986	6.23	6.09	0.01	8
PSO J338.2298+29.5089	5.35	7.68	0.25	5
VIK J2348–3054	2.64	4.33	0.05	8

Note. The corrected values have been calculated with Equation (19) and take into account the dependency on their luminosity. We also report the number of PCS adopted in the continuum fit.

2015a), which argued that the significant decrease of $R_{\rm NZ}$ with redshift could be explained by a steeply increasing IGM neutral fraction between $z \sim 5.7$ and 6.4.[28] The different trend of near-zone sizes with redshift with respect to what was found in the literature may be due to several reasons, i.e., we consider higher-quality spectra and a larger sample of quasars, we take into consideration a consistent definition of $R_{\rm NZ}$, and we do not exclude the WEL quasars at $z \sim 6$ (see Eilers et al. 2017, for an in-depth discussion of the discrepancies with previous works). We argue that the shallow evolution is due to the fact that $R_{\rm NZ,corr}$ does not depend entirely or only on the external IGM properties, but it correlates more strongly with the quasar characteristics (e.g., lifetime, regions of neutral hydrogen within the ionized zone), which are highly variable from object to object.

[28] We note that these studies considered a smaller and lower-z quasar sample, whose redshift measurements (mainly from the Mg II or Lyα emission lines, with only a minority of objects observed in CO or [C II]) have larger errors, and that they fit the redshift evolution of the near-zone sizes with a linear relation.

6. Discussion and Conclusions

In this work we present our search for z-dropouts in the third internal release of the Pan-STARRS1 stacked catalog (PS1 PV3), which led to the discovery of six new $z \sim 6.5$ quasars.

We complement these newly found quasars with all the other $z \gtrsim 6.5$ quasars known to date and perform a comprehensive analysis of the highest-redshift quasar population. In particular, we provide new optical/NIR spectroscopic observations for the six newly discovered quasars and for three sources taken from the literature (PSO 006+39, PSO 338+29, and HSC 1205); we also present new millimeter observations of the [C II] 158 μm emission line and the underlying continuum emission from NOEMA, for four quasars (PSO 006+39, PSO 323+12, PSO 338+12, and HSC 1205).

Our main results are as follows:

1. We calculate C IV rest-frame EWs, and blueshifts with respect to the Mg II emission line, for nine sources in our sample. We derive that all the $z \gtrsim 6.5$ quasars considered here show large blueshifts (740–5900 km s^{-1}), and they are outliers with respect to a comparison SDSS quasar sample at $z \sim 1$; they also have EW values equal to or lower than the ones of the low-redshift quasars. This evidence hints at a strong wind/outflow component in the BLRs of the highest-redshift quasars known.
2. We derive bolometric luminosities, black hole masses, and accretion rate estimates by modeling the Mg II emission line region ($2100 < \lambda$ [Å] < 3200) for 11 objects with available NIR spectroscopic observations. Comparing those measurements with the ones of a bolometric luminosity-matched quasar sample at lower redshift ($0.35 < z < 2.35$), we find that high-redshift quasars accrete their material at a similar rate, with a mean of $\langle \log(L_{\rm bol}/L_{\rm Edd}) \rangle \sim -0.41$ and a 1σ scatter of $\sim$0.4 dex, to their low-redshift counterparts, which present a mean of $\langle \log(L_{\rm bol}/L_{\rm Edd}) \rangle \sim -0.47$ and a

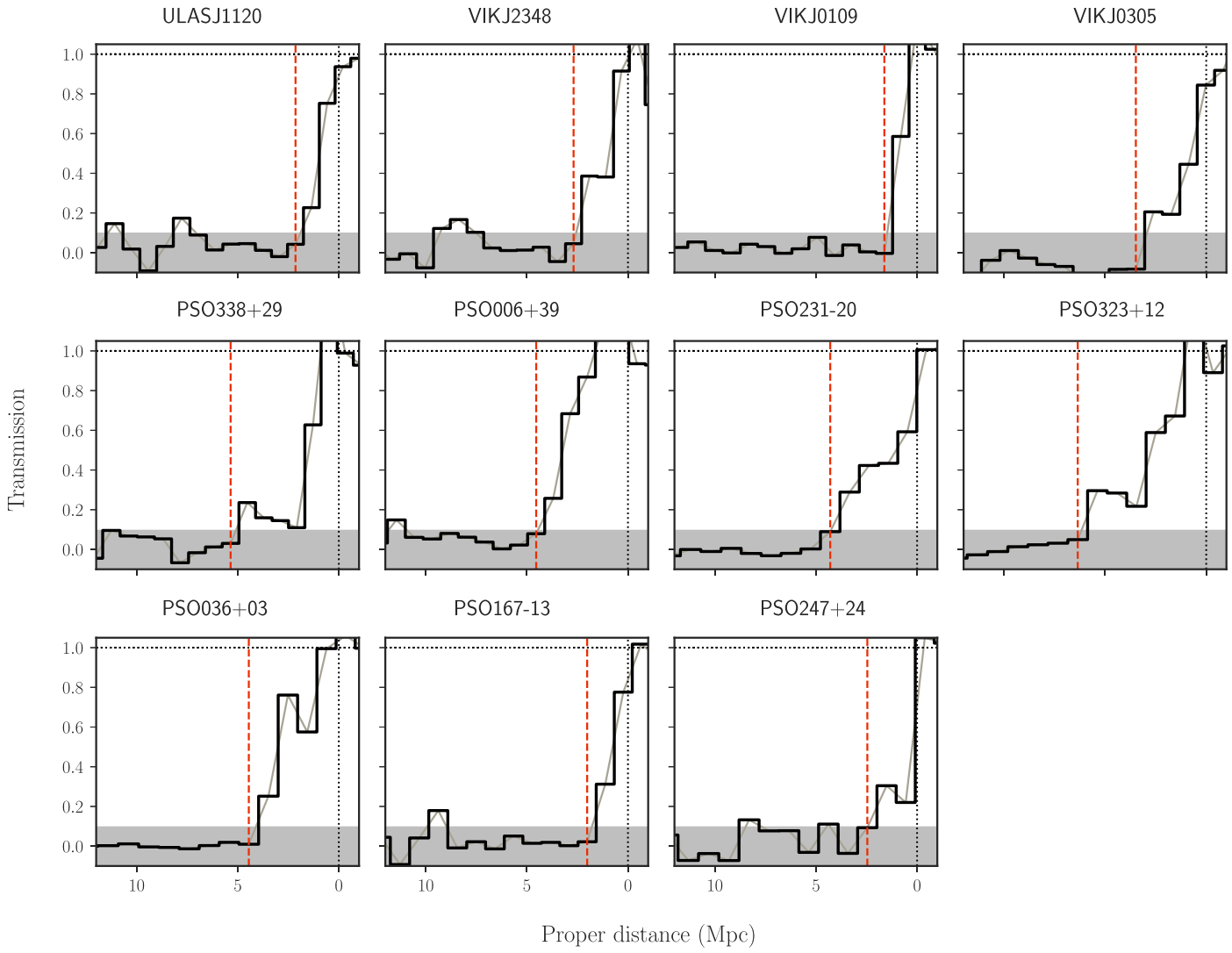

Figure 17. Transmission fluxes of the quasars in our sample, obtained normalizing the observed spectra by the emission model from the PCA method (see Section 4), as a function of proper distance from the source. We identify the near-zone radius (dashed red line) as the distance at which the flux drops below 10%, after smoothing each spectrum to a common resolution of 20 Å. We do not consider in our analysis HSC 1205, PSO 183+05, PSO 011+09, or PSO 261+19 (see text).

scatter of ∼0.3 dex. We also note that the high-redshift sample is biased toward higher luminosities: a more homogeneous coverage of the quasar parameter space at high redshift will help us investigate this evolution in the future.

3. We estimate the black hole seed masses ($M_{\rm BH,seed}$) required to grow the observed $z \gtrsim 6.5$ quasars studied here, assuming that they accrete at the constant observed Eddington ratio or with an Eddington ratio of unity, for a time equal to the age of the universe at the observed redshift, and with a constant radiative efficiency of 7%. In the first case, we derive $M_{\rm BH,seed} \gtrsim 10^4\ M_\odot$ (higher than what is expected in the collapse of Population III stars), while in the second case we obtain a lower value, consistent with all current theoretical models; this is valid even in the scenario where the seeds are formed at $z = 20$. Also, in the case in which the black hole seeds accrete at the Eddington rate with an efficiency of 10% from the beginning of the universe, their predicted masses are consistent with being formed by Population III stars. Alternatively, we calculate that if the seeds are created at $z \sim 20$–30 and accrete with $\epsilon = 0.1$, they would need to be as massive as $\gtrsim 10^{3\text{-}4}\ M_\odot$ (see Figure 13).
4. We calculate the Fe II/Mg II flux ratio, as a first-order proxy of the abundance ratio. We derive values systematically lower than the ones obtained for lower-redshift quasars, implying a decrease of the iron abundance at $z \gtrsim 6.4$. However, our measurements are hampered by large uncertainties, and, within these errors, we are consistent with a scenario of no evolution of the abundance ratio with redshift, as previously found by De Rosa et al. (2011, 2014) from a smaller sample of high-redshift quasars.
5. From new millimeter observations reported here for four objects, which completes the coverage of [C II] emission in quasars at $z > 6.5$, we derive precise redshift estimates ($\Delta z \lesssim 0.004$) and [C II] emission line and continuum luminosities, from which we obtain NIR and total infrared luminosities. We study the $L_{\rm [C\,II]}/L_{\rm FIR}$ ratio as a function of $L_{\rm FIR}$ for these sources, and we place them in the context of present measurements from the literature, for both high- and low-redshift objects, normal

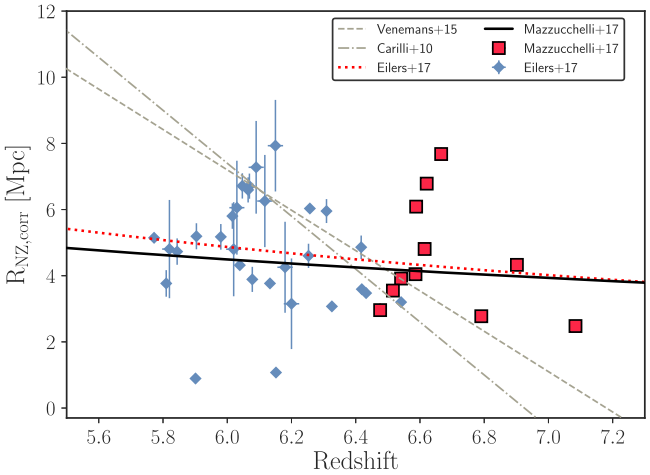

Figure 18. Near-zone size as a function of redshift for the objects in our sample (red squares), and the ones taken from Eilers et al. (2017; blue diamonds). The errors plotted are only due to the uncertainties on the redshifts, and for the quasars in this work they are particularly small owing to our precise $z_{[C\,II]}$ measurements (see Table 10). We fit the data with a power-law function (solid black line): the amplitude and slope values obtained are in line with the results presented by Eilers et al. (2017; red dotted line; see text and Equation (20)). We find a redshift evolution of the near-zone radii much shallower than that obtained in previous literature, e.g., by Carilli et al. (2010; dot-dashed line) and by Venemans et al. (2015a; gray dashed line). This could be explained by the fact that $R_{NZ,corr}$ depends more strongly on the individual quasar properties that vary from object to object, rather than on the overall characteristics of the IGM.

star-forming galaxies, LIRGs, ULIRGs, and quasars. We find that the values obtained cover a parameter space similar to that of ULIRGs.

6. We calculate the near-zone sizes of 11 objects. We study these measurements, together with the ones for a $5.6 \lesssim z \lesssim 6.5$ quasar sample from Eilers et al. (2017), as a function of redshift. The two data sets are analyzed with a consistent methodology; in agreement with Eilers et al. (2017), we find a much shallower evolution of the near-zone sizes with cosmic times than what was found by previous work (e.g., Carilli et al. 2010; Venemans et al. 2015a). This result is also in line with recent radiative transfer simulations (F. Davies et al., in preparation) and, as argued by Eilers et al. (2017), may be due to the much stronger dependency of the near-zone sizes on the particular quasar characteristics (e.g., age and/or islands of neutral gas located inside the ionized spheres) than on the general IGM properties.

The analysis presented here highlights the large variety of physical properties of the quasars at the highest redshifts accessible today and shows how these observations can address a number of crucial open issues. In the future, further statistical studies, supported by a larger sample of quasars (e.g., fainter sources and objects at higher redshift) and by observations with new transformational facilities (e.g., ALMA and *JWST*), will play a key role in our understanding of the universe at the very dawn of cosmic time.

We acknowledge the assistance of Mayte Alfaro and Nicolas Goody in some of the observations presented here.

E.P.F., B.P.V., and F.W. acknowledge funding through the ERC grant "Cosmic Dawn." Support for R.D. was provided by the DFG priority program 1573 "The Physics of the Interstellar Medium." C.M. thanks the IMPRS for Astronomy and Cosmic Physics at the University of Heidelberg.

The Pan-STARRS1 Surveys (PS1) have been made possible through contributions of the Institute for Astronomy, the University of Hawaii, the Pan-STARRS Project Office, the Max-Planck Society and its participating institutes, the Max Planck Institute for Astronomy, Heidelberg, and the Max Planck Institute for Extraterrestrial Physics, Garching, Johns Hopkins University, Durham University, the University of Edinburgh, Queen's University Belfast, the Harvard-Smithsonian Center for Astrophysics, the Las Cumbres Observatory Global Telescope Network Incorporated, the National Central University of Taiwan, the Space Telescope Science Institute, the National Aeronautics and Space Administration under grant no. NNX08AR22G issued through the Planetary Science Division of the NASA Science Mission Directorate, the National Science Foundation under grant no. AST-1238877, the University of Maryland, and Eotvos Lorand University (ELTE).

The present work is based on observations taken with ESO Telescopes at the La Silla Paranal Observatory, under the programs 092.A-0339(A), 092.A-0150(A), 092.A-0150(B), 093.A-0863(A), 095.A-9001(A), 095.A-0375(A), 095.A-0535(A), 095.A-0535(B), 096.A-0420(A), 096.A-9001(A), 097.A-9001(A), 097.A-0094(A), and 097.A-0094(B),

Part of the funding for GROND (both hardware and personnel) was generously granted from the Leibniz Prize to Prof. G. Hasinger (DFG grant HA 1850/28-1).

Part of the data presented herein were obtained at the W. M. Keck Observatory, which is operated as a scientific partnership among the California Institute of Technology, the University of California, and the National Aeronautics and Space Administration. The Observatory was made possible by the generous financial support of the W. M. Keck Foundation. The authors wish to recognize and acknowledge the very significant cultural role and reverence that the summit of Maunakea has always had within the indigenous Hawaiian community. We are most fortunate to have the opportunity to conduct observations from this mountain.

Some of the data here reported are based on observations collected at the Centro Astronómico Hispano Alemán at Calar Alto, jointly operated by the Max Planck Institute for Astronomy and the Instituto de Astrofisíca de Andalucía.

This paper includes data gathered with the 6.5 m Magellan Telescope located at Las Campanas Observatory, Chile. The FIRE observations were supported by the NFS under grant AST-1109915.

Part of the observations reported here were obtained at the MMT Observatory, a joint facility of the University of Arizona and the Smithsonian Institution.

The LBT is an international collaboration among institutions in the United States, Italy, and Germany. LBT Corporation partners are the University of Arizona on behalf of the Arizona university system; Istituto Nazionale di Astrofisica, Italy; LBT Beteiligungsgesellschaft, Germany, representing the Max-Planck Society, the Astrophysical Institute Potsdam, and Heidelberg University; The Ohio State University, and the Research Corporation, on behalf of the University of Notre Dame, University of Minnesota, and University of Virginia. This paper used data obtained with the MODS spectrographs built with funding from NSF

Table 11
List of Broadband Filters Used in This Work and Their Characteristics (Telescope/Survey, Central Wavelength, and Width)

Filter Name	Instrument/Survey	λ_c (μm)	$\Delta\lambda$ (μm)
g_{P1}	PS1	0.487	0.117
r_{P1}	PS1	0.622	0.132
i_{P1}	PS1	0.755	0.124
z_{P1}	PS1	0.868	0.097
y_{P1}	PS1	0.963	0.062
g_{decam}	DECaLS	0.475	0.152
r_{decam}	DECaLS	0.640	0.143
z_{decam}	DECaLS	0.928	0.147
Y	UKIDSS/VHS	1.000	0.120
J	UKIDSS/VHS	1.250	0.213
H	UKIDSS/VHS	1.650	0.307
K	UKIDSS/VHS	2.150	0.390
z_{O2K}	CAHA 3.5 m/Omega2000	0.908	0.158
Y_{O2K}	CAHA 3.5 m/Omega2000	1.039	0.205
J_{O2K}	CAHA 3.5 m/Omega2000	1.234	0.164
I_E	NTT/EFOSC2	0.793	0.126
Z_E	NTT/EFOSC2	>0.840	⋯
J_S	NTT/SofI	1.247	0.290
i_w	CAHA 3.5 m/CAFOS	0.762	0.139
i_{MMT}	MMT/MMTCam	0.769	0.130
Y_{retro}	du Pont/Retrocam	1.000	0.120
g_G	MPG 2.2 m/GROND	0.459	0.137
r_G	MPG 2.2 m/GROND	0.622	0.156
i_G	MPG 2.2 m/GROND	0.764	0.094
z_G	MPG 2.2 m/GROND	0.899	0.128
J_G	MPG 2.2 m/GROND	1.240	0.229
H_G	MPG 2.2 m/GROND	1.647	0.264
K_G	MPG 2.2 m/GROND	2.171	0.303
$W1$	ALLWISE	3.353	0.663
$W2$	ALLWISE	4.603	1.042

grant AST-9987045 and the NSF Telescope System Instrumentation Program (TSIP), with additional funds from the Ohio Board of Regents and the Ohio State University Office of Research.

This paper makes use of the following ALMA data: ADS/JAO.ALMA#2012.1.00882.S; ADS/JAO.ALMA#2015.1.01115.S. ALMA is a partnership of ESO (representing its member states), NSF (USA), and NINS (Japan), together with NRC (Canada), NSC and ASIAA (Taiwan), and KASI (Republic of Korea), in cooperation with the Republic of Chile. The Joint ALMA Observatory is operated by ESO, AUI/NRAO, and NAOJ.

This work includes observations carried out with the IRAM NOEMA Interferometer. IRAM is supported by INSU/CNRS (France), MPG (Germany), and IGN (Spain).

This publication makes use of data products from the *Wide-field Infrared Survey Explorer*, which is a joint project of the University of California, Los Angeles, and the Jet Propulsion Laboratory/California Institute of Technology, funded by the National Aeronautics and Space Administration.

This work is based in part on data obtained as part of the UKIRT Infrared Deep Sky Survey.

This research has benefited from the SpeX Prism Library, maintained by Adam Burgasser at http://www.browndwarfs.org/spexprism.

This research made use of Astropy, a community-developed core Python package for Astronomy (Astropy Collaboration, 2013; http://www.astropy.org).

Facilities: PS1 (GPC1), VLT:Antu (FORS2), NTT (EFOSC2, SofI), Max Planck.2.2m (GROND), Magellan:Baade(FIRE), Keck:I (LRIS), Hale (DBSP), CAO:3.5 m (Omega2000), CAO:2.2 m (CAFOS), DuPont (Retrocam), MMT (Red Channel Spectrograph), LBT (MODS).

Appendix A
Filters

We list in Table 11 the broadband filters used throughout this work, from both public surveys and follow-up campaigns.

Appendix B
Spectroscopically Rejected Objects

We report in Table 12 the Galactic contaminants found in our spectroscopic follow-up observations, which satisfied our

Table 12
Objects Spectroscopically Confirmed to Not Be High-redshift Quasars

Name	R.A. (J2000)	Decl. (J2000)	z_{P1}	y_{P1}	Y	J
PSO 229.40365–22.37078	229.403651	−22.3707877	>22.36	20.36 ± 0.14	…	20.95 ± 0.27
PSO 267.27554+15.6457	267.2755422	15.64579622	22.48 ± 0.31	20.69 ± 0.13	…	20.31 ± 0.18
PSO 357.24231+25.77427	357.2423123	25.77427024	>22.81	20.72 ± 0.13	21.52 ± 0.2	21.16 ± 0.14

selection criteria considering the PS1 PV3 database information (three sources). We list names, coordinates, z_{P1}, y_{P1}, Y, and J magnitudes. An accurate spectral classification of the sources is beyond the scope of this work.

ORCID iDs

C. Mazzucchelli https://orcid.org/0000-0002-5941-5214
E. Bañados https://orcid.org/0000-0002-2931-7824
B. P. Venemans https://orcid.org/0000-0001-9024-8322
R. Decarli https://orcid.org/0000-0002-2662-8803
E. P. Farina https://orcid.org/0000-0002-6822-2254
F. Walter https://orcid.org/0000-0003-4793-7880
A.-C. Eilers https://orcid.org/0000-0003-2895-6218
H.-W. Rix https://orcid.org/0000-0003-4996-9069
R. Simcoe https://orcid.org/0000-0003-3769-9559
D. Stern https://orcid.org/0000-0003-2686-9241
X. Fan https://orcid.org/0000-0003-3310-0131
E. Schlafly https://orcid.org/0000-0002-3569-7421
J. Hennawi https://orcid.org/0000-0002-7054-4332
K. C. Chambers https://orcid.org/0000-0001-6965-7789
W. Burgett https://orcid.org/0000-0003-4401-9582
P. W. Draper https://orcid.org/0000-0002-7204-9802
N. Kaiser https://orcid.org/0000-0001-6511-4306
E. Magnier https://orcid.org/0000-0002-7965-2815
N. Metcalfe https://orcid.org/0000-0001-9034-4402
C. Waters https://orcid.org/0000-0003-1989-4879
R. J. Wainscoat https://orcid.org/0000-0002-1341-0952

References

Alam, A., Albareti, F. D., Allende, P., et al. 2015, ApJS, 219, 12
Alexander, T., & Natarajan, P. 2014, Sci, 345, 1330
Alvarez, M., Wise, J. H., & Abel, T. 2009, ApJ, 701, 133
Appenzeller, I., Fricke, K., Fürtig, W., et al. 1998, Msngr, 94, 1
Bailer-Jones, C. A., Bizenberger, P., & Storz, C. 2000, Proc. SPIE, 4008, 1305
Baldwin, J. A. 1977, ApJ, 214, 679
Bañados, E., Decarli, R., Walter, F., et al. 2015, ApJ, 805, 8
Bañados, E., Venemans, B., Decarli, R., et al. 2016, ApJS, 227, 11
Bañados, E., Venemans, B., Morganson, E., Decarli, R., et al. 2014, AJ, 148, 14B
Barnett, R., Warren, S. J., Becker, G. D., et al. 2017, A&A, 601, 16
Barth, A. J., Martini, P., Nelson, C. H., & Ho, L. C. 2003, ApJ, 594, 95
Becker, G. D., Bolton, J. S., Madau, P., et al. 2015, MNRAS, 447, 3402
Beelen, A., Cox, P., Benford, D. J., et al. 2006, ApJ, 642, 694
Begelman, M. C., & Volonteri, M. 2017, MNRAS, 464, 1102
Bentz, M. C., Denney, K. D., Grier, C. J., et al. 2013, ApJ, 767, 149
Best, W. M. J., Liu, M. C., Magnier, E. A., et al. 2013, ApJ, 777, 84
Best, W. M. J., Liu, M. C., Magnier, E. A., et al. 2015, ApJ, 814, 118
Bond, J. R., Arnett, W. D., Carr, B. J., et al. 1984, ApJ, 280, 825
Brenneman, L. W., Reynolds, C. S., Nowak, M. A., et al. 2011, ApJ, 736, 103
Brisbin, D., Ferkinhoff, C., Nikola, T., et al. 2015, ApJ, 799, 13
Burgasser, A. J. 2014, in Int. Workshop on Stellar Spectral Libraries ASI Conf. Ser. 11, ed. H. P. Singh, P. Prugniel, & I. Vauglin (Bangalore: ASI), 7
Buzzoni, B., Delabre, B., Dekker, H., et al. 1984, Msngr, 38, 9
Calderone, G., Nicastro, L., Ghisellini, G., et al. 2017, MNRAS, 472, 4051
Calzetti, D., Armus, L., Bohlin, R. C., et al. 2000, ApJ, 533, 682
Carilli, C., & Walter, F. 2013, ARA&A, 51, 105
Carilli, C., Wang, R., Fan, X., et al. 2010, ApJ, 714, 834
Carnall, A. C., Shanks, T., Chehade, B., et al. 2015, MNRAS, 451, 16
Chambers, K., Magnier, E. A., Metcalfe, N., et al. 2016, arXiv:1612.05560C
Chen, S.-F. S., Simcoe, R., Torrey, P., et al. 2016, arXiv:1612.02829
Cox, P., Krips, M., Neri, R., et al. 2011, ApJ, 740, 63
De Breuck, C., Seymour, N., Stern, D., et al. 2011, A&A, 530, 8
De Rosa, G., Decarli, R., Walter, F., et al. 2011, ApJ, 739, 56
De Rosa, G., Venemans, B., Decarli, R., et al. 2014, ApJ, 790, 145
Decarli, R., Falomo, R., Treves, A., et al. 2010, MNRAS, 402, 2453
Decarli, R., Labita, M., Treves, A., & Falomo, R. 2008, MNRAS, 387, 1237
Devecchi, B., & Volonteri, M. 2009, ApJ, 694, 302
Diaz-Santos, T., Armus, L., Charmandairsm, V., et al. 2013, ApJ, 774, 68
Dubbeldam, M., Content, R., Allington-Smith, J. R., et al. 2000, Proc. SPIE, 4008, 1181
Eilers, A. C., Davies, F. B., Hennawi, J. F., Prochaska, J. X., & Mazzucchelli, C. 2017, ApJ, 840, 24
Fan, X., Strauss, M. A., Becker, R. H., et al. 2006, AJ, 132, 117
Fan, X., Strauss, M. A., Schneider, D. P., et al. 2003, AJ, 125, 1649
Fan, X., White, R. L., Davis, M., et al. 2000, AJ, 120, 1167
Farrah, D., Lebouteiller, V., Spoon, H. W. W., et al. 2013, ApJ, 776, 38
Flewelling, H. A., Magnier, E. A., Chambers, K. C., et al. 2016, arXiv:1612.05243
Gracia-Carpio, J., Sturm, E., Hailey-Dunsheath, S., et al. 2011, ApJ, 728, 7
Grandi, S. A. 1982, ApJ, 255, 15
Greig, B., Mesinger, A., Haiman, Z., & Simcoe, R. A. 2017, MNRAS, 466, 4239
Greiner, J., Bornermann, W., Clemens, C., et al. 2008, PASP, 120, 405
Grier, C. J., Peterson, B. M., Horne, K., et al. 2013, ApJ, 764, 47
Gullberg, B., De Breuck, C., Vieira, J. D., et al. 2015, MNRAS, 449, 2883
Haehnelt, M. G., & Rees, M. J. 1993, MNRAS, 263, 168
Helou, G., Khan, I., Iffat, R., et al. 1988, ApJS, 68, 151
Hewett, P. C., & Wild, V. 2010, MNRAS, 405, 2302
Ivison, R. J., Swinbank, A. M., Swinyard, B., et al. 2010, A&A, 518, 35
Iwamuro, F., Kimura, M., Eto, S., et al. 2004, ApJ, 614, 69
Iwamuro, F., Motohara, K., Maihara, T., et al. 2002, ApJ, 565, 63
Jiang, L., Fan, X., Vestergaard, M., et al. 2007, AJ, 134, 1150
Jiang, L., McGreer, I. D., Fan, X., et al. 2016, ApJ, 833, 222
Kaiser, N., Aussel, H., Burke, B. E., et al. 2002, Proc. SPIE, 4836, 154
Kaiser, N., Burgett, W., Chambers, K., et al. 2010, Proc. SPIE, 7733, 12
Kaspi, S., Maoz, D., Netzer, H., et al. 2005, ApJ, 629, 61
Kurk, J. D., Walter, F., Fan, X., et al. 2007, ApJ, 669, 32
Kurk, J. D., Walter, F., & Fan, X. 2009, ApJ, 702, 833
Lang, D. 2014, AJ, 147, 108
Langer, W. D., & Pineda, J. L. 2015, A&A, 580, 5
Latif, M., & Ferrara, A. 2016, PASA, 33, 51
Latif, M. A., & Schleicher, D. R. G. 2015, A&A, 578, 118
Lawrence, A., Warren, S. J., Almaini, O., et al. 2007, MNRAS, 379, 1599
Leighly, K. M. 2004, ApJ, 11, 125
Lupi, A., Haardt, F., Dotti, M., et al. 2016, MNRAS, 456, 2993
Madau, P., Haardt, F., & Dotti, M. 2014, ApJ, 784, 38
Magnier, E. A., Chambers, K. C., Flewelling, H. A., et al. 2016a, arXiv:1612.05240
Magnier, E. A., Schlafly, E. F., Finkbeiner, D. P., et al. 2016b, arXiv:1612.05244
Magnier, E. A., Sweeney, W. E., Chambers, K. C., et al. 2016c, arXiv:1612.05242
Mainzer, A., Bauer, J., Grav, T., et al. 2011, ApJ, 731, 53
Maiolino, R., Caselli, P., Nagao, T., et al. 2009, A&A, 500, L1
Maiolino, R., Cox, P., Caselli, P., et al. 2005, A&A, 440, 51
Maiolino, R., Juarez, Y., Mujica, R., et al. 2003, ApJ, 596, 155
Malhotra, S., Kaufman, M. J., Hollenbach, D., et al. 2001, ApJ, 561, 766
Marconi, A., Axon, D. J., Maiolino, R., et al. 2008, ApJ, 678, 693
Matsuoka, Y., Onoue, M., Kashikawa, N., et al. 2016, ApJ, 828, 26
Matsuoka, Y., Onoue, M., Kashikawa, N., et al. 2017, arXiv:1704.05854
Matteucci, F., & Greggio, L. 1986, A&A, 154, 279
Matthews, J. H., Knigge, C., & Long, K. S. 2017, MNRAS, 467, 2571
McGreer, I., Mesinger, A., & D'Orico, V. 2015, MNRAS, 447, 499
McMahon, R. J., Banerji, M., Gonzalez, E., et al. 2013, Msngr, 154, 35
Meiksin, A. 2006, MNRAS, 365, 807
Meisner, A. M., Lang, D., & Schlegel, D. J. 2016, AAS Meeting Abstracts, #227, 140.03

Moorwood, A., Cuby, J. G., & Lidman, C. 1998, Msngr, 91, 9
Morganson, E., De Rosa, G., Decarli, R., et al. 2012, AJ, 143, 142
Mortlock, D. J., Patel, M., Warren, S. J., et al. 2009, A&A, 505, 97
Mortlock, D. J., Warren, S. J., Venemans, B., et al. 2011, Natur, 474, 616
Nomoto, K., Hashimoto, M., Tsujimoto, T., et al. 1997, NuPhA, 616, 79
Oke, J. B., Cohen, M., Carr, J., et al. 1995, PASP, 107, 375
Oke, J. B., & Gunn, J. E. 1982, PASP, 107, 375
Onken, C. A., Ferrarese, L., Merritt, D., et al. 2004, ApJ, 615, 645O
Pacucci, F., Volonteri, M., & Ferrara, A. 2015, MNRAS, 452, 1922
Palanque-Delabrouille, N., Yeche, C., Borde, A., et al. 2013, A&A, 559, 85
Pâris, I., Petitjean, P., Aubourg, E., et al. 2014, A&A, 563, 54
Pâris, I., Petitjean, P., Rollinde, E., et al. 2011, A&A, 530, 50
Pâris, I., Petitjean, P., Ross, N. P., et al. 2017, A&A, 597, 79
Peterson, B. M., Ferrarese, L., Gilbert, K. M., et al. 2004, ApJ, 613, 682
Pezzulli, E., Valiante, R., & Schneider, R. 2016, MNRAS, 458, 3047
Planck Collaboration, Ade, P. A. R., Aghanim, N., et al. 2016, A&A, 594, 13
Pogge, R. W., Atwood, B., Brewer, D. F., et al. 2010, Proc. SPIE, 7735, 9
Reed, S. L., McMahon, R. G., Banerji, M., et al. 2015, MNRAS, 454, 3952
Reed, S. L., McMahon, R. G., Martini, P., et al. 2017, MNRAS, 468, 4702
Reynolds, C. S. 2014, SSRv, 183, 277
Richards, G. T., Kruczek, N. E., Gallagher, S. C., et al. 2011, AJ, 141, 167
Richards, G. T., Vanden Berk, D. E., Reichard, T. A., et al. 2002, AJ, 124, 1
Riechers, D. A., Bradford, C. M., Clements, D. L., et al. 2013, Natur, 496, 329
Rockosi, C., Stover, R., Kibrick, R., et al. 2010, Proc. SPIE, 7735, 0
Sameshima, H., Maza, J., Matsuoka, Y., et al. 2009, MNRAS, 395, 1087
Sargsyan, L., Lebouteiller, V., Weedman, D., et al. 2014, ApJ, 755, 171
Schlegel, D. J., Finkbeiner, D. P., & Davis, M. 1998, ApJ, 500, 525
Schmidt, G. D., Weynmann, R. J., & Foltz, C. B. 1989, PASP, 101, 713
Schneider, D. P., Fan, X., Hall, P. B., et al. 2005, AJ, 126, 2579
Selsing, J., Fynbo, J. P. U., Christensen, L., & Krogager, J. K. 2016, A&A, 585, 87
Sesana, A., Barausse, E., Dotti, M., & Rossi, E. M. 2014, ApJ, 794, 104
Shao, Y., Wang, R., Jones, G. C., et al. 2017, ApJ, 845, 138
Shapiro, S. L. 2005, ApJ, 620, 59
Shen, Y., Greene, J. E., Strauss, M., et al. 2008, ApJ, 680, 169
Shen, Y., Richards, G. T., Strauss, M. A., et al. 2011, ApJS, 194, 45
Simcoe, R. A., Burgasser, A. J., Bernstein, R. A., et al. 2008, Proc. SPIE, 7014, 70140
Skrzypek, N., Warren, S. J., Faherty, J. K., et al. 2015, A&A, 574, 78
Stacey, G. J., Hailey-Dunsheath, S., Ferkinhoff, C., et al. 2010, ApJ, 724, 957
Stern, D., Hall, P. B., Barrientos, F. L., et al. 2003, ApJ, 596, 39
Suzuki, N. , 2006, ApJS, 163, 121
Tang, J. J., Goto, T., Ohyama, Y., et al. 2017, MNRAS, 466, 4568
Valiante, R., Schneider, R., Volonteri, M., & Omukai, K. 2016, MNRAS, 457, 3356
Valtchanov, I., Virdee, J., Ivison, R. J., et al. 2011, MNRAS, 415, 3473
Vanden Berk, D. E., Richards, G. T., Bauer, A., et al. 2001, AJ, 122, 549
Venemans, B. P., Bañados, E., Decarli, R., et al. 2015, ApJ, 801, 11
Venemans, B. P., Findlay, J. R., Sutherland, W. J., et al. 2013, ApJ, 779, 24
Venemans, B. P., McMahon, R. G., Walter, F., et al. 2012, ApJ, 751, 25
Venemans, B. P., McMahon, R. G., Warren, S. J., et al. 2007, MNRAS, 376, 76
Venemans, B. P., Verdoes Kleijn, G. A., Mwebaze, J., et al. 2015, MNRAS, 453, 2259
Venemans, B. P., Walter, F., Decarli, R., et al. 2017, ApJ, 837, 146
Venemans, B. P., Walter, F., Zschaechner, L., et al. 2016, ApJ, 816, 37
Vernet, J., Dekker, H., D'Orico, S., et al. 2011, A&A, 536, 105
Vestergaard, M., & Osmer, P. S. 2009, ApJ, 699, 816
Vestergaard, M., & Wilkes, B. J. 2001, ApJS, 134, 1
Volonteri, M. 2010, A&ARv, 18, 279
Volonteri, M., Habouzit, M., Pacucci, F., & Tremmel, M. 2016, IAUS, 319, 72
Volonteri, M., & Rees, M. J. 2005, ApJ, 633, 624
Wagg, J., Carilli, C. L., Wilner, D. J., et al. 2010, A&A, 519, 1
Wagg, J., Wiklind, T., Carilli, C. L., et al. 2012, ApJ, 752, 30
Walter, F., Bertoldi, F., Carilli, C., et al. 2003, Natur, 424, 406
Walter, F., Decarli, R., Carilli, C., et al. 2012, Natur, 486, 233
Walter, F., Riechers, D., Cox, P., et al. 2009, Natur, 457, 699
Walton, D. J., Reynolds, M. T., Miller, J. M., et al. 2015, ApJ, 805, 161
Wang, F., Fan, X., Yang, J., et al. 2017, ApJ, 839, 27
Wang, F., Wu, X. B., Fan, X., et al. 2016, ApJ, 819, 24
Wang, R., Wagg, J., Carilli, C. L., et al. 2011, AJ, 142, 101
Wang, R., Wagg, J., Carilli, C. L., et al. 2013, ApJ, 773, 44
Waters, C. Z., Magnier, E. A., Price, P. A., et al. 2016, arXiv:1612.05245
West, A. A., Morgan, D. P., Bochanski, J. J., et al. 2011, in ASP Conf. Ser. 448 (San Francisco, CA: ASP), 1407
Willott, C. J., Albert, L., Arzoumanian, D., et al. 2010a AJ, 140, 560
Willott, C. J., Bergeron, J., & Omont, A. 2015, ApJ, 801, 123
Willott, C. J., Delorme, P., & Omont, A. 2007, AJ, 134, 2435
Willott, C. J., Delorme, P., & Reyle, C. 2009, AJ, 137, 3541
Willott, C. J., Delorme, P., Reyle, C., et al. 2010b AJ, 139, 906
Willott, C. J., Omont, A., & Bergeron, J. 2013, ApJ, 770, 13
Wright, E. L., Eisenhardt, P. R. M., Mainzer, A. K., et al. 2010, AJ, 140 1868
Wu, X. B., Wang, F., Fan, X., et al. 2015, Natur, 518, 512